Chemical degradation of magnesium potassium phosphate cement pastes during leaching by demineralized water: Experimental investigation and modeling

Laura Diaz Caselles, Céline Cau Dit Coumes, Pascal Antonucci, Angélique Rousselet, A. Mesbah, V. Montouillout

Cement and Concrete Research 178 (2024) 107456

Contents lists available at ScienceDirect

Cement and Concrete Research

journal homepage: www.elsevier.com/locate/cemconres

Chemical degradation of magnesium potassium phosphate cement pastes during leaching by demineralized water: Experimental investigation and modeling

Laura Diaz Caselles [a,*], Céline Cau Dit Coumes [a], Pascal Antonucci [a], Angélique Rousselet [b], Adel Mesbah [c], Valérie Montouillout [d]

[a] CEA, DES, ISEC, DPME, SEME, Univ Montpellier, Marcoule, France
[b] Université Paris-Saclay, CEA, Service de recherche en Corrosion et Comportement des Matériaux, 91191 Gif-sur-Yvette, France
[c] Univ Lyon, Université Lyon 1, Institut de Recherches sur la Catalyse et l'Environnement de Lyon, IRCELYON, UMR5256, CNRS, Villeurbanne, France
[d] CNRS, CEMHTI UPR3079, Univ. Orléans, F-45071 Orléans, France

ARTICLE INFO

Keywords:
Magnesium phosphate cement
Durability
Leaching
Reactive transport modeling

ABSTRACT

The long-term durability of magnesium potassium phosphate cement (MKPC) pastes was investigated by examining their leaching behavior. MKPC comprised magnesium oxide (MgO) and potassium dihydrogen phosphate (KH_2PO_4) in equimolar amounts and yielded K-struvite ($MgKPO_4{\cdot}6H_2O$) and a nearly neutral pore solution pH upon hydration. Semi-dynamic leaching tests were performed on MKPC paste samples using demineralized water with a pH set at 7, and the leached solids were analyzed using XRD, SEM/EDS, ^{11}B and ^{31}P MAS-NMR spectroscopy. Leaching was mainly governed by diffusion of dissolved species through the pore network of the paste. Three main zones were observed in the leached solids: (*i*) a poorly cohesive residual layer where K-struvite was fully depleted, (*ii*) an intermediate zone where K-struvite coexisted with cattiite ($Mg_3(PO_4)_2{\cdot}22H_2O$), and (*iii*) a third zone without any cattiite. Reactive transport modeling made it possible to predict the extent of degradation and the phase evolution in the MKPC paste samples.

1. Introduction

The reprocessing of nuclear spent fuel from first-generation nuclear reactors (natural uranium – graphite – gas type) has produced waste containing aluminum (Al) metal that must be stabilized and solidified before final disposal. Portland cement (PC) is commonly used for conditioning low- or intermediate-level radioactive waste [1]. However, its high alkalinity is problematic for Al stabilization due to metal corrosion and dihydrogen release [2,3]. To improve the long-term stability of radioactive waste containing Al metal, alternative materials must be explored. Magnesium phosphate cements (MPCs) are promising alternatives to PC as their nearly neutral pore solution may lead to passivation of Al metal [3–5]. MPCs have divers applications beyond Al waste encapsulation, including heavy metal immobilization and stabilization/solidification of radioactive waste, due to the formation of insoluble phosphate compounds across a wide range of pH [6–8]. In civil engineering, MPCs have also been used as rapid-repair materials for building and transport applications, such as roads, runways, pavements, and highways, because of their fast-setting properties [9–11]. In addition, MPCs have been studied as bone cements for biological applications [12–14].

MPCs are formed by the reaction between MgO and a soluble acidic phosphate salt such as potassium dihydrogen phosphate (KH_2PO_4), sodium dihydrogen phosphate (NaH_2PO_4), or ammonium dihydrogen phosphate ($NH_4H_2PO_4$) [15–18]. When their primary constituents are MgO and KH_2PO_4, the resulting materials are referred to as magnesium potassium phosphate cements (MKPCs). In equimolar amounts, the hydration of MKPCs yields K-struvite ($MgKPO_4{\cdot}6H_2O$), a low-solubility mineral that can exist in both crystalline and poorly crystalline (amorphous) forms, setting the pore solution pH to nearly neutral values (i.e., within the passivation domain of Al metal) [3,18,19]. Additionally, newberyite ($MgHPO_4{\cdot}3H_2O$), phosphorrösslerite ($MgHPO_4{\cdot}7H_2O$), bobierrite ($Mg_3(PO_4)_2{\cdot}8H_2O$), and cattiite ($Mg_3(PO_4)_2{\cdot}22H_2O$) have been identified during hydration [18,20,21]. The formation of these

* Corresponding author.
E-mail addresses: laura.diazcaselles@cea.fr (L. Diaz Caselles), celine.cau-dit-coumes@cea.fr (C. Cau Dit Coumes), pascal.antonucci@cea.fr (P. Antonucci), angelique.rousselet@cea.fr (A. Rousselet), adel.mesbah@ircelyon.univ-lyon1.fr (A. Mesbah), valerie.montouillout@cnrs-orleans.fr (V. Montouillout).

https://doi.org/10.1016/j.cemconres.2024.107456
Received 30 October 2023; Received in revised form 22 December 2023; Accepted 2 February 2024
Available online 7 February 2024

phases depends on several parameters such as the water-to-cement (w/c) ratio, the Mg/P molar ratio, and the presence or absence of any retarders (e.g., $B(OH)_3$) or impurities [19,22]. Despite the potential benefits of MKPCs for the stabilization of waste containing Al metal, information on their long-term durability is still limited. Lahalle et al. [23] investigated the microstructural and mineralogical evolution over time of MKPC paste samples with a Mg/P molar ratio of 1 and a w/c of 0.56 immersed in deionized water (pH 6.8) for 6 months. XRD analyses showed that the crystalline K-struvite content tended to decrease whereas the amorphous content of the material increased, likely due to the formation of poorly crystalline K-struvite (or amorphization of existent K-struvite). Pore solution extraction showed that pH was about 8.5, similar to the one measured before immersion. In addition, the release of ions, particularly potassium, was evidenced into the immersion solution. Several studies have shown that the compressive strength of MPC-based materials tends to decrease in contact with water [24–27]. For instance, Yang et al. [24] investigated the water resistance of MPC mortars prepared with $NH_4H_2PO_4$ and a Mg/P molar ratio of 3. Mortars, firstly cured for 28 days under endogenous conditions, showed a strength decrease of approximately 11 % and 18 % when immersed for 30 and 90 days, respectively. These results suggest that the microstructure of MPC-based materials may vary in contact with water. Therefore, it is important to understand the degradation mechanisms of these binders under leaching to design materials with improved durability. This study aims to (*i*) investigate the leaching behavior of MKPC paste samples using demineralized water under well-controlled conditions, and (*ii*) contribute to the understanding of their degradation mechanisms using both experimental and modeling approaches.

To this end, the leaching behavior of MKPC paste samples was assessed by performing semi-dynamic leaching tests using demineralized water with a pH set at 7 using a titrator working in the pH-stat mode. Renewal of the leaching solutions was carried out over time to prevent the accumulation of dissolved species. The leachates were analyzed by inductively coupled plasma atomic emission spectroscopy (ICP-AES). The leached solids were characterized using several techniques including X-ray diffraction (XRD), scanning electron microscopy with energy-dispersive X-ray spectroscopy (SEM/EDS), and magic angle spinning solid-state nuclear magnetic resonance (MAS-NMR). Furthermore, experimental data were used as input for numerical simulations using a reactive transport model.

2. Materials and methods

2.1. Materials

2.1.1. Raw materials

The chemical compositions of the raw materials were determined using semi-quantitative X-ray fluorescence (XRF) using a Bruker S.8 spectrometer. Results are presented in Table 1.

- A hard-burnt magnesium oxide (MgO – purity above 98.3 %) was used in this study and purchased from Martin Marietta Magnesia specialties (MagChem® 10CR). It presented a monomodal particle size distribution, with $d_{10} = 4.8$ μm, $d_{50} = 18.9$ μm and $d_{90} = 45.6$ μm, and a specific surface area (BET) of 0.9 m^2/g.
- Potassium dihydrogen phosphate (KH_2PO_4) ($d_{10} = 139$ μm, $d_{50} = 303$ μm, and $d_{90} = 566$ μm) was purchased as a fertilizer from YARA (KristaTM, purity >98 %).
- A low calcium oxide fly ash (siliceous fly ash V, according to EN 197–1, $d_{10} = 7$ μm, $d_{50} = 31$ μm, and $d_{90} = 163$ μm, specific surface area (BET) of 1.5 m^2/g) was obtained from EDF (power station from Cordemais, France) and used to improve the rheological properties and stability of the mixtures. XRD Rietveld analyses indicated that fly ash comprised 72.4 wt% amorphous content, 17.2 wt% mullite and 10.4 wt% quartz.
- Boric acid ($B(OH)_3$) was used as set retarder. It was purchased from VWR with reference number 20177 and a purity over 98 %.

2.1.2. Sample preparation and curing

MKPC pastes were prepared using a Mg/PO_4 molar ratio of 1 and a water-to-cement (w/c) weight ratio of 0.51 (cement: MgO + KH_2PO_4). The choice of a Mg/PO_4 molar ratio of 1 was made for two reasons. First, it helped maintain the pore solution pH below 11, which is important to mitigate Al metal corrosion. Secondly, it prevented the presence of excessive residual MgO that could potentially hydrate at a later stage and cause expansion due to the formation of brucite ($Mg(OH)_2$). As for the w/c ratio, the value of 0.51 corresponds to the chemical water demand of the binder (i.e., the theoretical minimum water content needed to achieve full hydration of cement yielding K-struvite) based on the mass balance equation presented in Eq. (1):

$$MgO + KH_2PO_4 + 5\,H_2O \rightarrow MgKPO_4.6H_2O \quad (1)$$

Fly ash and boric acid were added at constant fly ash/cement and boric acid/cement weight ratios of 1 and 0.02, respectively. Boric acid was first dissolved in demineralized water. The pre-mixed dried solids (anhydrous MgO, KH_2PO_4, and fly ash) were then added to the boric acid solution and mixed for 5 min at low speed in a standardized mixer according to EN 196-3. The resulting paste was cast into hermetic, and cylindrical plastic containers measuring 8 cm in length and 5 cm in diameter to follow an endogenous cure and to avoid desiccation. All the containers were placed in a chamber controlled at 20 °C. The samples were stored for six months until characterization and leaching. The mix design of the pastes is presented in Table 2.

2.2. Methods

2.2.1. Leaching tests

Three semi-dynamic leaching tests were carried out for periods of 28, 90, and 210 days. Therefore, the sample before leaching and the leached solids will be referred to as MKP-ref, MKP-28d, MKP-90d, and MKP-210d, respectively.

The leaching solution was demineralized water with a pH maintained at 7 by adding small aliquots of 0.5 M nitric acid (HNO_3) using a titrator (Titroline 7000 using TitriSoft software - version 3.5.0/3.5.0 P) operating in the pH-stat mode. Frequent calibrations of the pH electrode were performed using standard buffer solutions at pH 6.865 ± 0.01 (25 °C) and pH 9.180 ± 0.01 (25 °C) to avoid any shift over the duration

Table 2
Mix design of MKPC pastes. Values are given in grams, for 1 L of material.

	MgO	KH_2PO_4	Fly ash	Boric acid	Water[a]	w/c[b]
MKPC	131.4	443.6	575.0	11.5	293.2	0.51

[a] Demineralized water.
[b] Water-to-cement weight ratio (cement: MgO + KH_2PO_4).

Table 1
Chemical compositions of the raw materials, obtained by semi-quantitative XRF. Values are given in % by weight.

	SiO_2	Al_2O_3	Fe_2O_3	CaO	K_2O	TiO_2	Na_2O	MgO	P_2O_5	SO_3	Cl^-
MgO	0.3	–	0.3	0.9	–	–	–	98.5	–	–	–
KH_2PO_4	–	–	–	–	40.0	–	–	–	59.3	0.5	0.1
Fly ash	57.8	24.7	6.0	4.5	2.2	1.3	0.7	1.6	0.6	0.5	0.1

of the experiments. The experimental setup was designed to get unidirectional diffusion of the leaching solution, thus making it possible to use a one-dimension (1D) reactive transport model to analyze the results. To ensure this unidirectional diffusion, the lateral surface of the cylinder paste samples was coated with an epoxy resin, while the parallel extremities were kept exposed (Fig. 1). The sample (one per test) was suspended in a double-walled reactor, which was pre-filled with 1.7 L of demineralized water and maintained at a constant temperature of 25 °C. The liquid volume-to-solid surface (L/S) ratio was equal to 43.29 cm. Magnetic stirring was employed throughout the test to prevent any local concentration effect. To avoid any carbonation of the solution, nitrogen (N_2)-saturated water was injected by bubbling into the reactor. To prevent the accumulation of dissolved species in the leaching solution, periodic renewals were carried out at specific intervals, namely 4 ± 1 days, 7 ± 1 days, 18 ± 2 days, and then every 10 days throughout the entire duration of the tests. The total amount of HNO_3 added by titration between two renewals was always inferior to 1 % of the initial volume of demineralized water (i.e., <17 mL HNO_3). Leachates were filtered using 0.2 µm membranes, and diluted using a 2 vol% HNO_3 solution at factors of 10 or 100. Concentrations of dissolved K, P, Mg, B, Ca, Si, S, Na, Al, Fe, Ti and Mn were determined by ICP-AES. Fig. 1 displays a scheme of the leaching device.

2.2.2. Characterization of porosity in the reference sample

After six months of curing and before leaching, the total porosity accessible to mercury and the pore size distribution were determined in the reference sample (MKP-ref) using Mercury Intrusion Porosimetry (MIP) with an AutoPore IV 9500 Porosimeter from Micromeritics Instrument Corporation, following ISO 15901-1 (2005) standard. To this end, MKP-ref was immersed in isopropanol and gently dried in a desiccator at 20 °C and 20 % R.H. MIP analyses were then performed on small pieces of paste of approximately 1–3 g. The mercury pressure varied from 0.0014 MPa to 400 MPa, and the pore entry size diameters were >3 nm. In addition, total porosity accessible to water was determined in MKP-ref according to NF P 18-459 (2010). Three paste samples (5 cm diameter and 2 cm height) were placed in a vacuum desiccator at 25 mbar for 4 h. Then, samples were covered with demineralized water while maintaining the vacuum pressure at 25 mbar for a minimum of 44 h. After the immersion period, suspended and saturated weights of samples were determined. Samples were dried to a constant weight in an oven controlled at 38 °C and 10 % R.H. to preserve the integrity of the K-struvite phase, which is unstable at higher temperatures [21,23].

2.2.3. Sample preparation and X-ray diffraction (XRD) analyses

Paste samples were characterized using Powder-XRD analyses both before and after leaching. Prior to leaching, XRD analyses were performed on samples that were submitted to hydration stoppage through solvent exchange with isopropanol as recommended by RILEM TC-238 SCM [28]. To eliminate any residual isopropanol, samples were stored in a desiccator maintained at 20 °C and 20 % R.H. for 7 days. Pastes were then manually ground to a particle size smaller than 63 µm. After leaching, pastes were simply rinsed with isopropanol. Next, the powder was manually recovered from different depths by carefully abrading the surface of samples using SiC abrasive paper, step by step, starting from the exposed surface towards the core. The difference in thickness was determined in each step using a digital caliper with a measurement range of 0–25 mm and an accuracy of 0.001 mm.

For the PXRD analyses, a PANalytical X'Pert Pro diffractometer equipped with a PIXcel detector and a copper radiation source (Cu $K\alpha_{1,2}$, $\lambda = 1.54184$ Å) was use in order to reduce the preferred orientation effect, data were collected in transmission mode (Debye-Scherrer) using a capillary with an external diameter of 0.7 mm and a wall thickness of 0.01 mm. Scans were conducted over a 2θ angular range from 5° to 120° with a step size of 2θ 0.013° and a time per step of 2.35 s. Pure silicon was collected in similar conditions and used to extract the instrumental function. In addition, about 10 wt% pure silicon (Si) was added to each sample as an internal standard to evaluate the amount of crystalline

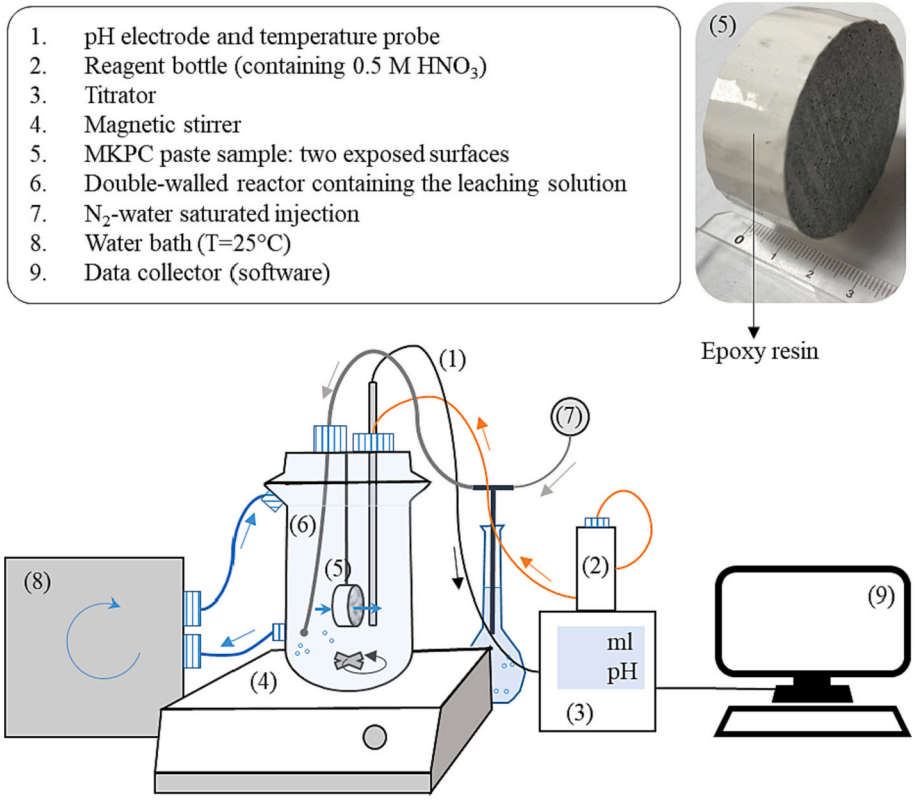

Fig. 1. Scheme of the device used for the leaching experiments.

phases and amorphous. To avoid any errors related to the difference in absorption factors between the different phases, the fully crystalline phases (except for fly ash) were mixed with 10 wt% Si and refined separately to estimate the Brindley factor. Identification of the phases was performed using Diffrac.Suite Eva and/or Highscore softwares. The Rietveld refinement was performed using the Fullprof_suite program [29]. During the refinement, multiple profile and structure parameters were allowed to vary, such as zero shift, unit cell parameters, B overall factor, preferred orientation and scale factor. The broadening effect was refined using an anisotropic size model. After refining the content of each phase (wt%), the amount of the amorphous phase was estimated from the ratio between the amount of silicon found after the refinement and initial value of 10 wt%

2.2.4. SEM/EDS analyses

After curing and prior to leaching, hydration stoppage was performed on paste samples as described in Section 2.2.3. After leaching, samples were delicately rinsed with isopropanol and cut into small pieces using a diamond wire saw. Microstructure analyses were then conducted on carbon-coated fractures and polished sections using a Scanning Electron Microscope (SEM) FEI Inspect S50 equipped with an Electron dispersive spectroscopy (EDS) detector (Bruker XFlash SDD 10 mm^2). Scattered and backscattered electron (SE and BSE) configurations were used to obtain images, applying magnifications ranging from 50× to 2000×. Moreover, EDS mapping was conducted to estimate the depth of the degraded layer and the changes in its elemental composition. In addition, EDS point analyses were performed to characterize the phase evolution in the solid fraction, with an average of 150 analyses taken per sample. Calibration for quantification was achieved using a set of eleven reference standards: jadeite $NaAl(Si_2O_6)$, magnesium oxide (MgO, 99.95 % pure), aluminum oxide (Al_2O_3, 99.8 % pure), orthoclase ($KAlSi_3O_8$), wollastonite ($CaSiO_3$), titanium (Ti, 99.99 % pure), chromium (Cr, 99.96 % pure), manganese (Mn, 99.99 %), iron (Fe, 99.95 % pure), pyrite (FeS_2), and gallium phosphide (GaP, 99.99 % pure).

2.2.5. MAS NMR analyses

Solid state magic angle spinning nuclear magnetic resonance (MAS NMR) was used to characterize MKPC paste and to investigate changes in the P and B environments before and after leaching. ^{31}P and ^{29}Si spectra were acquired on a Bruker AVANCE III spectrometer ($B_0 = 9.4$ T) operating at 162 MHz and 79.4 MHz for ^{31}P and ^{29}Si respectively. For ^{31}P spectra, the spinning speed was fixed at 20 kHz and 384 scans were accumulated after a single short pulse ($\pi/4$) and a recycling delay of 360 s ensuring complete magnetization relaxation. In the case of ^{29}Si spectra, the rotation was limited at 8 kHz, and almost 34,000 scans were added with a recycling delay of 10 s.

^{27}Al and ^{11}B spectra were obtained on a Bruker AVANCE NEO spectrometer ($B_0 = 20$ T) operating at 221.6 MHz and 272.8 MHz for ^{27}Al and ^{11}B, respectively using a spinning speed of 30 kHz. ^{27}Al spectrum was acquired after a short pulse ($\pi/18$) ensuring a homogeneous excitation, 10,240 scans were added using a recycling delay of 1 s. Finally, ^{11}B spectra were acquired using a Hahn-echo pulse sequence to remove the probe signal. 20,324 scans were accumulated with a recycling delay of 10 s. Nevertheless, despite the 2.3 days of acquisition time, the spectrum remained very noisy, making accurate quantification impossible. The chemical shifts were referenced relative to H_3PO_4 85 %, $BF_3O(C_2H_5)_2$, $Al(NO_3)_3$ and trimethylsilane for ^{31}P, ^{11}B, ^{27}Al and ^{29}Si, respectively. Quantitative analyses of the ^{31}P MAS NMR spectra were performed using the Dmfit program developed at CEMHTI [30].

2.2.6. Estimation of pH in the cement pastes

A pH-indicator was used to estimate the pH of cement pastes before and after leaching. To this end, the Rainbow indicator was purchased from German Instruments. This indicator has broad pH ranges: orange (pH 4–6), yellow (pH 6–8), green (pH 8–10), purple (pH 10–12), and blue (pH 12–14). In order to measure the pH of paste samples, the indicator was sprayed on the cross-section of either broken pieces or cut samples. Pictures of sprayed surfaces were taken after a few minutes when the indicator solution was dried.

2.3. Modeling approach

2.3.1. HYTEC: reactive transport code

Leaching of paste samples was simulated in time using a 1D model (i.e., unidirectional diffusion) developed with HYTEC reactive transport code (version 4.7.4) [31]. This code takes into account the migration of ions through the cementitious material (transport by diffusion) and the associated geochemical reactions (using the geochemical module CHESS). Diffusion is coupled to chemistry as described by Eq. (2) [32].

$$\frac{\partial \omega c_i}{\partial t} = \nabla.(D_e \nabla c_i) - \frac{\partial \omega \overline{c}_i}{\partial t} \quad (2)$$

In Eq. (2), c_i represents the mobile concentration of a specie per unit volume of solution, while $\overline{c}_i$ represents the immobile concentration. Additionally, ω denotes the porosity, and D_e stands for the effective diffusion coefficient. The determination of the solid fraction involves chemical calculations, while the aqueous fraction is calculated by transport processes. Therefore, transport and chemistry are coupled through a sequential iterative algorithm simultaneously considering the alteration fronts caused by mineral dissolution, and the associated ion release from the paste. Furthermore, alterations in local porosity due to mineral precipitation or dissolution lead to changes in the D_e value. To incorporate the retroactive effect of chemistry on mass transport, a modified version of Archie's law was implemented in the HYTEC code, as described by Eq. (3) [32].

$$D_e(\omega) = D_e(\omega_0)\left(\frac{\omega - \omega_c}{\omega_0 - \omega_c}\right)^{\alpha} \quad (3)$$

In Eq. (3), ω_0 stands for the initial porosity, which was determined experimentally on the sound material before leaching. The critical porosity threshold under which diffusion stops is denoted as ω_c. Additionally, α represents an empirical Archie's coefficient. A ω_c value of 0 and an Archie's coefficient α ranging from 1.5 to 4 have been commonly used to model the degradation of cementitious materials [32–35]. In this study, an Archie's power of 2.0 provided satisfactory fit of the experimental results.

2.3.2. Description of model setup

Fig. 2 illustrates the computational domain defined in this study, which comprised two zones: (*i*) the MKPC paste sample, and (*ii*) the reactor containing the leaching solution. As shown in Fig. 2, the geometry of the MKPC paste was represented as a rectangle (50 mm by height, 10 mm by length), which corresponded to half of the experimental thickness of the experimental sample to reduce the computation time. The reactor was also modeled as a rectangle with 50 mm height and 434 mm length to reproduce the experimental liquid volume-to-solid surface (L/S) ratio of 43.29 cm since the code automatically assumes a depth of 1 m in the z-axis. The grid regime was defined in one direction using a vertical mesh. The node size of the calculation grid were set at 100 μm in the paste and in the first 10 mm of the reactor zone (zone b in Fig. 2), then it increased at 1 mm. The leaching solution comprised water with a pH set at 7, and a diffusivity coefficient of 1.0×10^{-5} $m^2 \cdot s^{-1}$ was employed to simulate a homogeneous and agitated solution. No boundary conditions were defined in this model. Additionally, the leaching solution was renewed at the same frequency as in the experiments. The chemical reactions were computed by assuming local thermodynamic equilibrium and using the B-dot activity model for ionic strength correction.

2.3.3. Thermodynamic data

The thermodynamic CHESS database (version 2.5) was used in this simulation and enriched with thermodynamic data for magnesium

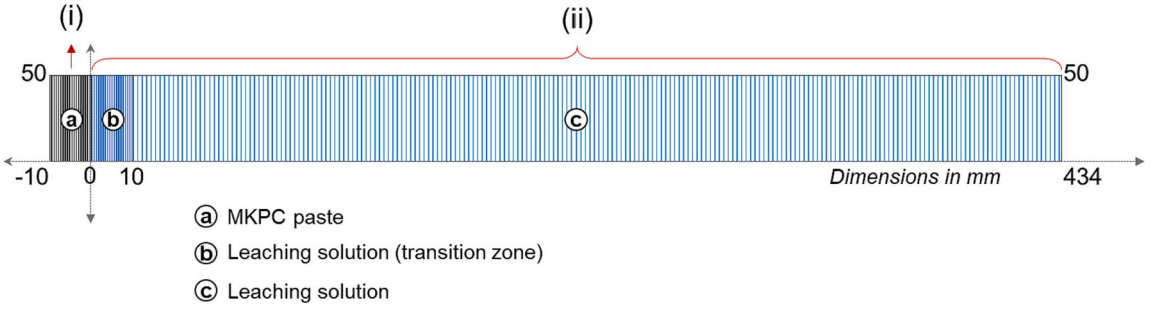

Fig. 2. Computational domain (i) MKPC paste, and (ii) the reactor zone containing the leaching solution. Node size grid: (a), (b) 100 μm, and (c) 1 mm.

phosphate phases presented in the literature. The minerals considered are presented in Table 3.

3. Experimental results

3.1. Characterization of the reference paste

MKP-ref was characterized using XRD prior to leaching. MKP-ref was mainly composed of K-struvite ($MgKPO_4{\cdot}6H_2O$), along with residual MgO, quartz, mullite (silicate mineral), and an amorphous fraction responsible for a broad hump centered at approximately 2θ 22 ° (see blue pattern at the bottom of Fig. 9). Quartz and mullite were present in the fly ash added to the mixture and the amorphous content was ascribed to fly ash, but also possibly to transient magnesium phosphates and/or poorly crystallized K-struvite [19,23]. XRD Rietveld refinement resulted in 53.8 wt% K-struvite, 1.8 wt% MgO, 8.2 wt% mullite, 2.6 wt% quartz, and 33.6 wt% amorphous content.

Fig. 3 shows the ^{31}P, ^{29}Si and ^{27}Al MAS-NMR spectra obtained from MKP-ref after hydration stoppage (Section 2.2.3). In addition, Table 4 presents the results of quantitative analyses of the ^{31}P MAS-NMR spectrum, where the average chemical shifts and line widths were measured for each signal contribution.

The ^{31}P MAS-NMR spectrum of MKP-ref (Fig. 3a) displayed three distinct signal contributions corresponding to different P chemical environments. The dominant sharp resonance at δ = +6.5 ppm corresponded to an orthophosphate and was assigned to K-struvite, in agreement with literature reports [22,37,38]. A small ^{31}P resonance at δ = +4.1 ppm was associated with residual KH_2PO_4 [22,37], which represented 1 % of the ^{31}P fraction (Table 4). This means that KH_2PO_4 was not fully exhausted after 6 months of curing. The broad hump signal ranging from δ = +10 ppm to −10 ppm and centered at δ = +0.9 ppm was not clearly assigned to any specific compound. However, it may correspond to one or several contributions of poorly crystallized phosphate phases, such as:

(i) $Mg_2KH(PO_4)_2{\cdot}15H_2O$, which has been reported to present several resonances at δ = +2.6 ppm, +3.1 ppm, +3.4 ppm, and +3.7 ppm [22],
(ii) lünebergite ($Mg_3B_2(PO_4)_2(OH)_6{\cdot}6H_2O$), which is a poorly crystallized borophosphate with a chemical shift at δ = −2.7 ppm [22],
(iii) an anhydrous poorly crystallized orthophosphate $Mg_3(PO_4)_2$, which has a chemical shift ranging from δ = +0.6 ppm to δ = −0.5 ppm [38]. Alternatively, it could also be attributed to hydrated magnesium phosphate phases ($Mg_3(PO_4)_2{\cdot}xH_2O$), which exhibit chemical shifts at δ = −0.73 ppm, −0.89 ppm, −2.69 ppm, and −3.03 ppm [39].

On the ^{29}Si MAS-NMR spectrum (Fig. 3b), the signal extended from −80 to −115 ppm. Due to the low signal/noise ratio, only the thin signal of quartz (δ = −110 ppm) can be clearly distinguished. This contribution was very probably underestimated, as quantifying it would require much longer recycling times. The rest of the signal corresponded to the different silicon environments of the vitreous part of fly ash and mullite [40–42]. The ^{27}Al MAS-NMR spectrum (Fig. 3c), showed the presence of several aluminum species in 4-fold and 6-fold coordination, centered around 57 ppm and 4 ppm, respectively. The signals were complex and would have required additional experiments to be simulated. However, according to the literature, these signals could be assigned to the aluminum environments in mullite present in fly ash [43].

SEM/EDS analyses of MKP-ref revealed the presence of abundant K-struvite, which exhibited micro-cracks likely resulting from drying due to the high vacuum in the SEM chamber (Fig. 4). In addition, fly ash grains were found all over MKP-ref matrix. The darker grey zones in the BSE images corresponded to the presence of unreacted MgO. Furthermore, a bright phase containing S and K, possibly K_2SO_4, was also identified in MKP-ref (Fig. 4c). The total S content in the paste matrix was about 0.13 wt%, of which 47.1 % was found to come from the addition of fly ash, while the remaining 52.9 % came from impurities detected in the KH_2PO_4 used to prepare the pastes (Table 1).

EDS point analyses of MKP-ref (excluding fly ash grains) are presented as K/P vs. Mg/P mixing diagrams (Fig. 5a). The Mg/P and K/P atomic ratios were plotted on the x- and y-axis, respectively. This figure includes the expected regions for different phases that could be present in the MKPC paste samples upon hydration, such as residual KH_2PO_4, K-

Table 3
Thermodynamic data at 25 °C and 1 bar.

Species	Reaction	Log $K_{formation}$	Vol (kg/m^3)	Ref.
K-struvite	$Mg^{2+} + HPO_4^{2-} + K^+ + 6H_2O \rightarrow MgKPO_4{\cdot}6H_2O + H^+$	−1.36	1870.2	[21]
Cattiite	$3Mg^{2+} + 2HPO_4^{2-} + 22H_2O \rightarrow Mg_3(PO_4)_2.22H_2O + 2H^+$	−1.61	1640.5	[21]
$Mg_2KH(PO_4)_2.15H_2O$	$2Mg^{2+} + 2HPO_4^{2-} + K^+ + 15H_2O \rightarrow Mg_2KH(PO_4)_2.15H_2O + H^+$	4.03	1810.6	[21]
Phosphorrösslerite	$Mg^{2+} + HPO_4^{2-} + 7H_2O \rightarrow MgHPO_4.7H_2O$	4.69	1740.3	[21]
Newberyite	$Mg^{2+} + HPO_4^{2-} + 3H_2O \rightarrow MgHPO_4.3H_2O$	5.61	2121.1	[21]
$MgKPO_4.H_2O$	$Mg^{2+} + HPO4^{2-} + K^+ + H_2O \rightarrow MgKPO_4.H_2O + H^+$	−1.37	2668.7	[21]
Farringtonite	$3Mg^{2+} + 2HPO_4^{2-} \rightarrow Mg_3(PO_4)_2 + 2H^+$	−2.23	2761.2	[21]
Bobierrite	$3Mg^{2+} + 2HPO_4^{2-} + 8H_2O \rightarrow Mg_3(PO_4)_2{\cdot}8H_2O + 2H^+$	0.66	2129.9	[21]
Magnesium orthophosphate tetrahydrate	$3Mg^{2+} + 2HPO_4^{2-} + 4H_2O \rightarrow Mg_3(PO_4)_2{\cdot}4H_2O + 2H^+$	−1.14	2380.6	[21]
Lünebergite	$3Mg^{2+} + 2HPO_4^{2-} + 2B(OH)_3 + 6H_2O \rightarrow Mg_3B_2(PO_4)_2(OH)_6{\cdot}6H_2O + 2H^+$	−99.25	–	[36]

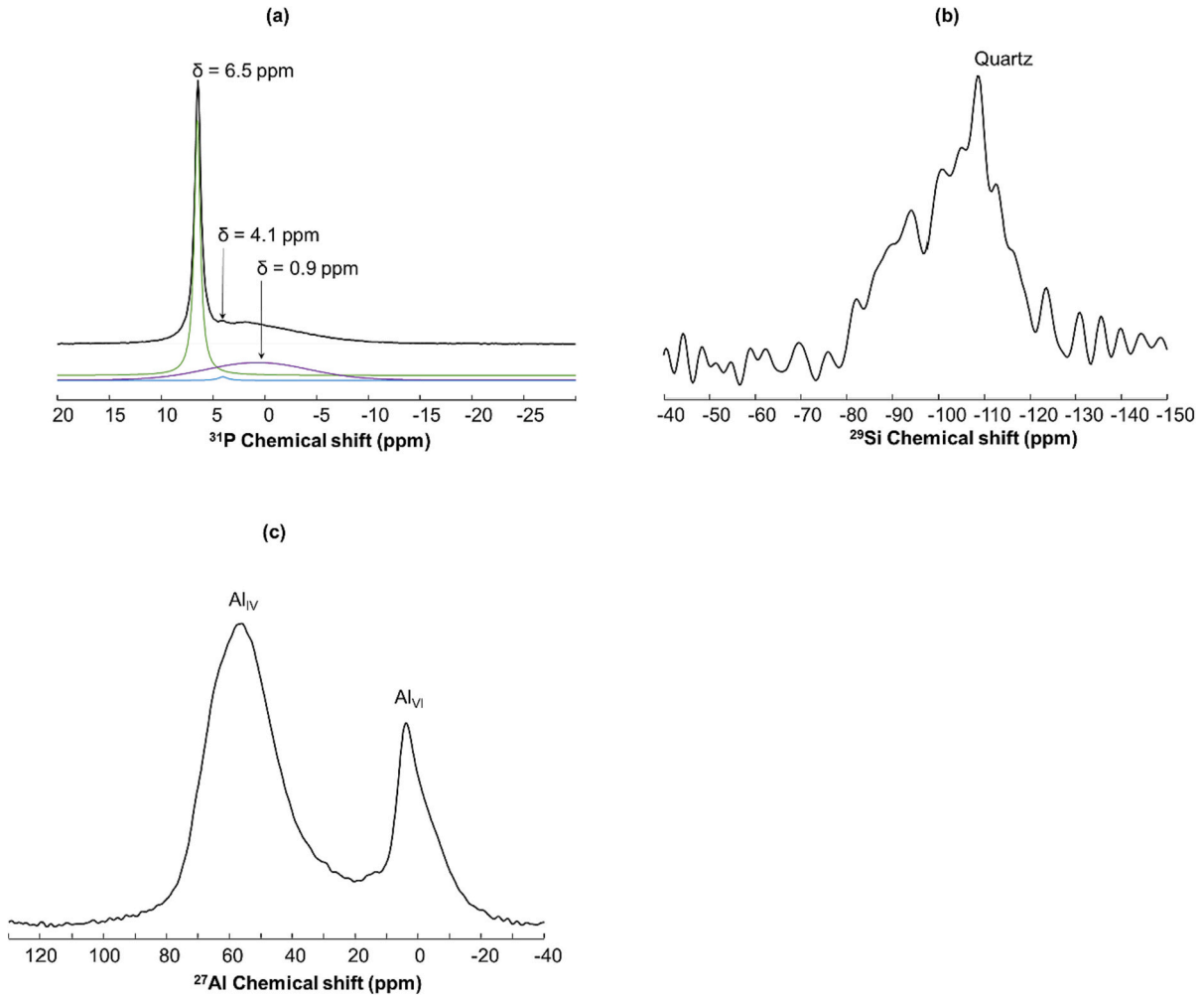

Fig. 3. MKP-ref (a) ^{31}P MAS-NMR. (b) ^{29}Si MAS NMR, and (c) ^{27}Al MAS NMR. δ indicates chemical shift. Black lines correspond to experimental spectra, and colored lines to single sites evidenced by decomposition.

Table 4
^{31}P site fractions (mol. %) estimated from decomposition ^{31}P spectrum in MKP-ref.

	Assignment	Chemical shift (ppm)	Width (ppm)	^{31}P fraction (%)
MKP-ref	K-struvite ($MgKPO_4{\cdot}6H_2O$)	+6.5	0.7	76
	Residual KH_2PO_4	+4.1	1.0	1
	Broad hump (?)*	+0.9	10.2	23
MKP-90d	K-struvite	+6.6	1.3	43
	Broad hump (?)*	+2.2	9.0	57

(?)*These signals were not clearly assigned to any specific compound.

struvite, $Mg_2KH(PO_4)_2{\cdot}15H_2O$, bobierrite ($Mg_3(PO_4)_2{\cdot}8H_2O$), cattiite ($Mg_3(PO_4)_2{\cdot}22H_2O$), phosphorrösslerite ($MgHPO_4{\cdot}7H_2O$), newberyite ($MgHPO_4{\cdot}3H_2O$), magnesium hydrogen phosphate ($Mg(H_2PO_4)_2{\cdot}xH_2O$ or $MgH_2P_2O_7$), brucite ($Mg(OH)_2$), and $CaK_3H(PO_4)_2$ [21,22].

MKP-ref presented a population of EDS points with Mg/P and K/P atomic ratios comprised between 0.5 and 1.0, slightly deviating from the expected ratios of 1 for K-struvite. This result suggested the coexistence, at the submicronic level, of K-struvite and $Mg_2KH(PO_4)_2{\cdot}15H_2O$ or other poorly crystalline phosphate phases as suggested by ^{31}P MAS-NMR analyses (Fig. 3). The deviation of K/Mg and K/P atomic ratios from unity may also be explained by the presence of the phase rich in S and K (Fig. 4c) or by the residual presence of MgO and KH_2PO_4, as detected by XRD and ^{31}P MAS-NMR spectroscopy (Figs. 9 and 3). EDS point analyses confirmed the absence of any phosphösslerite or newberyite, which have Mg/P and K/P atomic ratios of 1 and 0, respectively.

Some studies have suggested the potential of fly ash to react upon hydration of MKPC samples [25,37]. However, in this study, no clear correlation between Al-Si-P or Al-Si-Mg contents was found by EDS point analyses.

The total porosity accessible to mercury (15.2 %) was consistent with the total porosity accessible to water (15.5 ± 0.2 %). The distribution of pore entry diameters revealed that MKP-ref presented a wide range of pore size diameters (Fig. 6). The highest population of pore size diameters (31 %) ranged between 0.01 and 0.1 μm, meanwhile 11 % of the distribution corresponded to large pore size diameters (>100 μm).

3.2. Leaching of MKPC paste samples: experimental results

3.2.1. Composition of the leachates

Fig. 7 presents the evolution of the cumulative leached concentrations (in mmol/L) of K, P, Mg, B, S, Si and Ca as a function of the square root of time (in days$^{1/2}$) for leaching tests carried out for 28, 90 and 210 days. Moreover, Table 5 displays the initial composition of the MKPC paste sample along with the cumulative leached elemental concentrations (in mmol/g of paste) determined for all leaching periods. The data were calculated using a density value of 1876.2 kg/m^3 for the cement paste (obtained by total porosity accessible to water experiments).

Table 6 gives the slopes values for cumulative K, P, Mg and B concentrations. Slopes were calculated with the first 5 points of each curve,

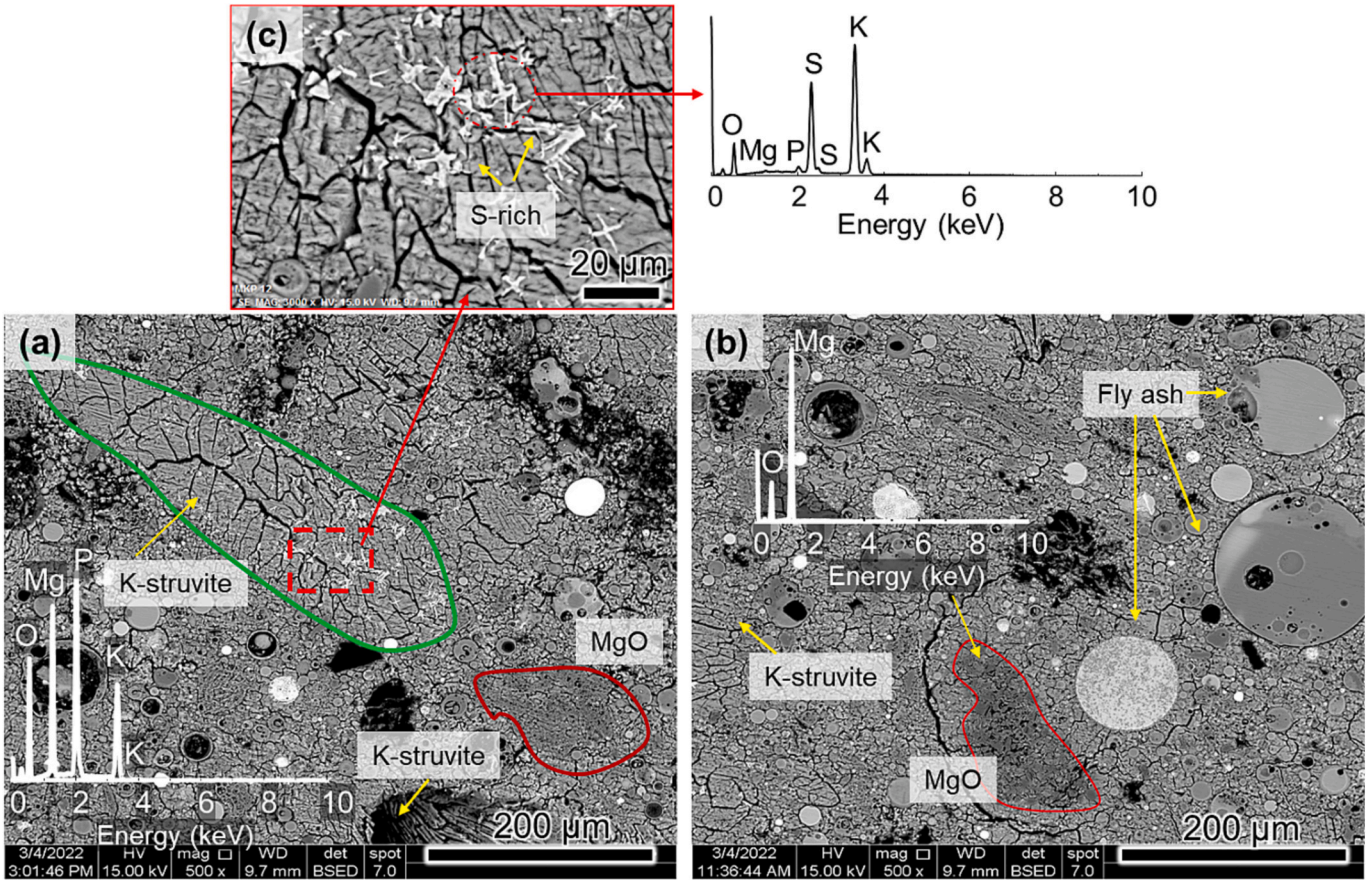

Fig. 4. MKP-ref (a), (b) SEM images of a polished cross-section, and (c) zoom-in view of K-struvite showing the presence of a sulfur and potassium-rich phase.

which represent the first stage of leaching for each experiment.

Leaching tests presented a good repeatability (Fig. 7 and Table 6), except for the quantification of Si in the leachates, possibly due to heterogeneities in the soluble fraction of fly ash. The leaching of samples using demineralized water resulted in a continuous release of elements into the solution, leading to a gradual increase in elemental concentrations in the leachates (Fig. 7). The leaching of K was considerably higher than that of P, which in turn exceeded that of Mg. B and S were completely depleted from the matrix at the end of the longest leaching experiment, meaning that the minerals containing S and B (including the bright S- and K-rich phase evidenced by SEM) were highly soluble.

As shown in Fig. 7h, the cumulative concentration of HNO_3 injected by titration increased linearly with the square root of time, indicating the release of basic aqueous species such as PO_4^{3-} and OH^-, resulting from the dissolution of K-struvite and MgO. Similar linear evolutions were observed for the cumulative concentrations of Mg, Ca, as well as S and B until their exhaustion from the solid. As for K and P, two linear regimes were successively observed, with a change occurring after 28 days of leaching. This transition could result from the exhaustion of both the dissolved species in the pore solution and the soluble phases containing K and/or P, such as residual KH_2PO_4, accounting for 1 mol% of the ^{31}P fraction (Table 4). In addition, leaching of soluble K present in fly ash or in impurities could also be involved in the first 28 days (Fig. 4).

Regardless of the test duration, the K/Mg and P/Mg flux ratios (equal to 3.6 and 2.0, respectively) strongly deviated from 1, thus indicating that the release of Mg, K and P did not simply result from congruent dissolution of K-struvite $MgKPO_4.6H_2O$, but resulted from a combination of different processes.

3.2.2. Mineralogical evolution of leached solids

After leaching, paste samples were recovered and rinsed with isopropanol, and the thickness of each sample was measured using a digital caliper. The exposed surfaces of all samples were friable, and the epoxy resin was easily removed, without any observed cracking or swelling (Fig. 8). The thickness of leached samples decreased over time, meaning that surface erosion occurred, leading to progressive loss of material and interface retreat (interface = exposed surface). The interface retreat seemed to increase linearly with the square root of time (Fig. 8). Extrapolating this trend would lead to an interface retreat of approximately 2.6 mm after 1 year of leaching.

Moreover, the pH of leached samples was estimated using the Rainbow indicator. The cross-sections of leached pastes exhibited a red-purple color on the sprayed regions, indicating that pH increased from 8 to a value between 10 and 12.

3.2.2.1. XRD analyses. Fig. 9 presents the XRD patterns of MKP-28d obtained at various depths and ranging from the exposed surface to the core. The patterns are displayed in of 5°-40° 2θ range to emphasize the main differences. Fig. 10 illustrates the mineralogical assemblage evolution in depth determined by Rietveld refinement in MKP-28d. Similar phase evolutions were observed for the samples leached for 90 days and 210 days, but over different depth scales.

XRD patterns of leached solids (Fig. 9) revealed the existence of three distinct zones:

- *Zone 1 or residual layer*: located at the exposed surface of the samples, where the leaching solution-to-solid surface interface is placed. The thickness of the residual layers was irregular all along the exposed surfaces and found to be approximately 225 ± 62 µm, 145 ± 35 µm, and 98 ± 28 µm for MKP-28d, MKP-90d and MKP-210d, respectively. The residual layers only exhibited two crystalline phases: mullite and quartz coming from fly ash (see the XRD pattern in the

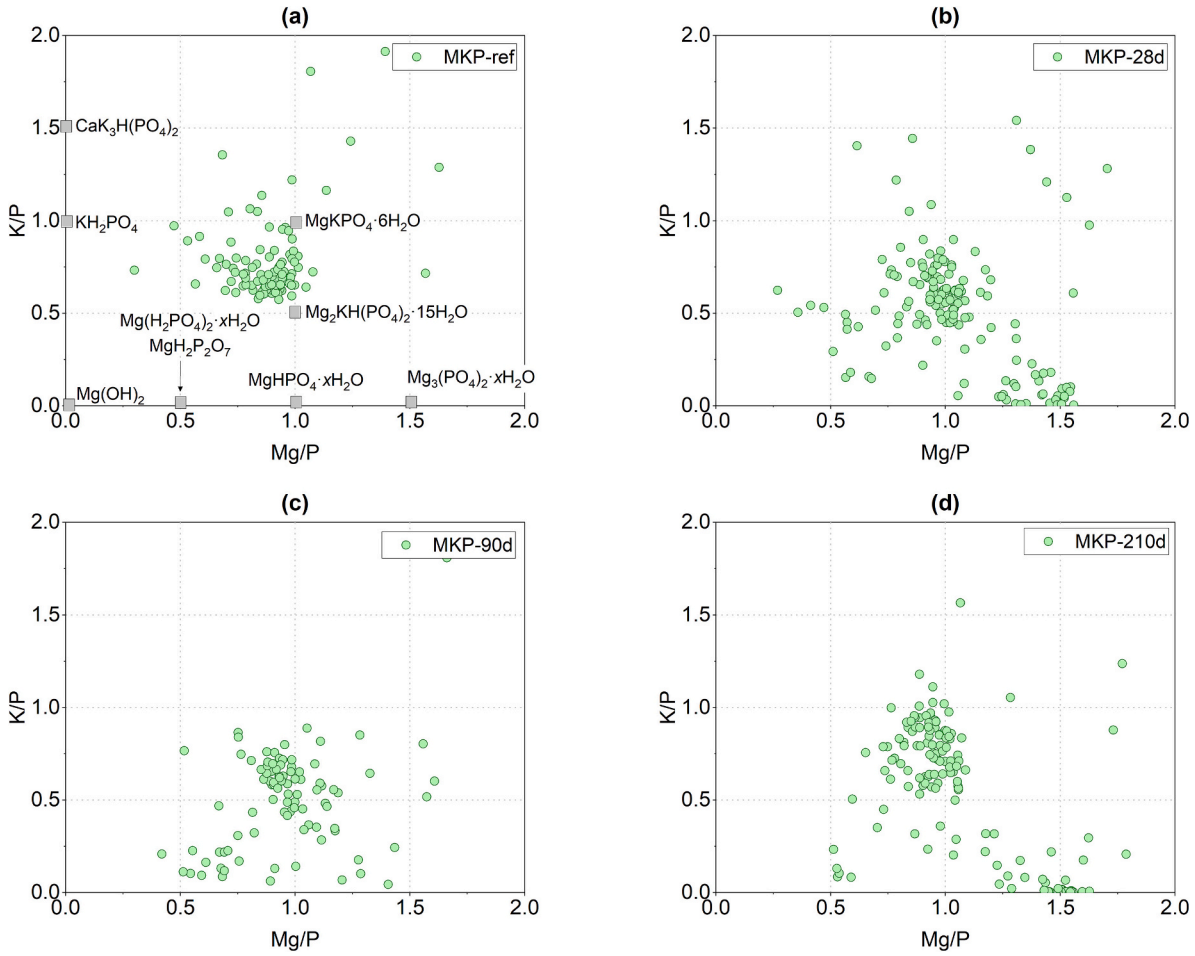

Fig. 5. EDS mixing diagrams of K/P vs Mg/P atomic ratios of polished cross-sections (a) MKP-ref, and leached solids: (b) MKP-28d, (c) MKP-90d, and (d) MKP-210d.

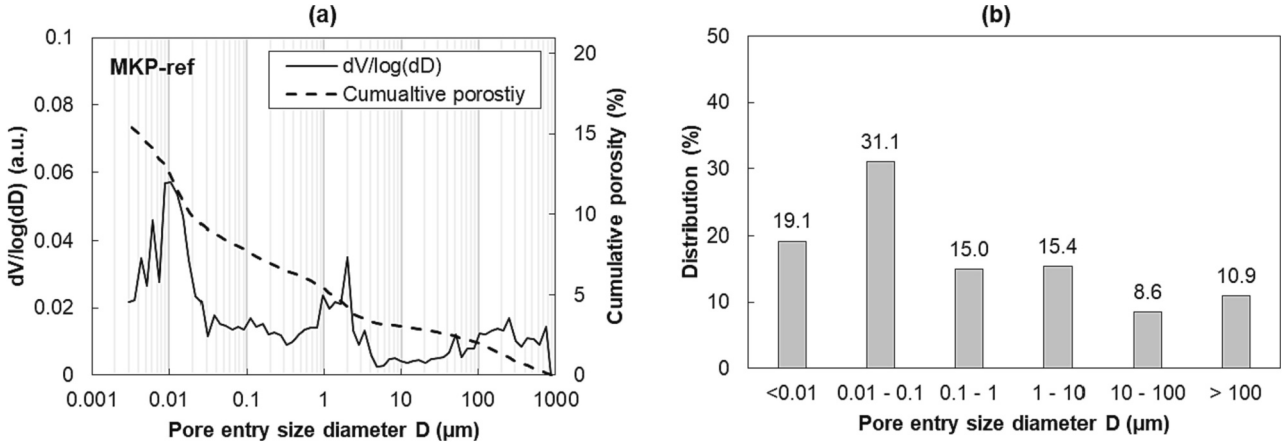

Fig. 6. MKP-ref (a) cumulative MIP porosity and first derivative results, and (b) distribution of the pore entry size diameter.

bottom in Fig. 9). This means that K-struvite was fully depleted in this zone. Furthermore, a broad amorphous hump centered at 2θ 22° was identified, corresponding to 77 wt% amorphous fraction.

- *Zone 2 or intermediate zone*: XRD patterns showed peaks of both crystalline K-struvite and cattiite ($Mg_3(PO_4)_2{\cdot}22H_2O$), in addition to mullite and quartz. The amount of K-struvite content decreased near the exposed surface, whereas the content of amorphous increased. Peaks of cattiite were identified up to a depth of 1.5 ± 0.1 mm in MKP-28d, 2.8 ± 0.1 mm in MKP-90d and 3.0 ± 0.1 mm in MKP-210d. Cattiite is a potassium-free magnesium phosphate phase. Its precipitation in zone 2 could contribute to explain why the flux of K released in solution was notably higher than that of P.
- *Zone 3*: the XRD patterns recorded in this zone did not exhibit any peaks of cattiite. Nevertheless, Rietveld refinement showed a fluctuation in K-struvite and amorphous content, suggesting the possible dissolution of K-struvite and its reprecipitation near the transition between zones 2 and 3.

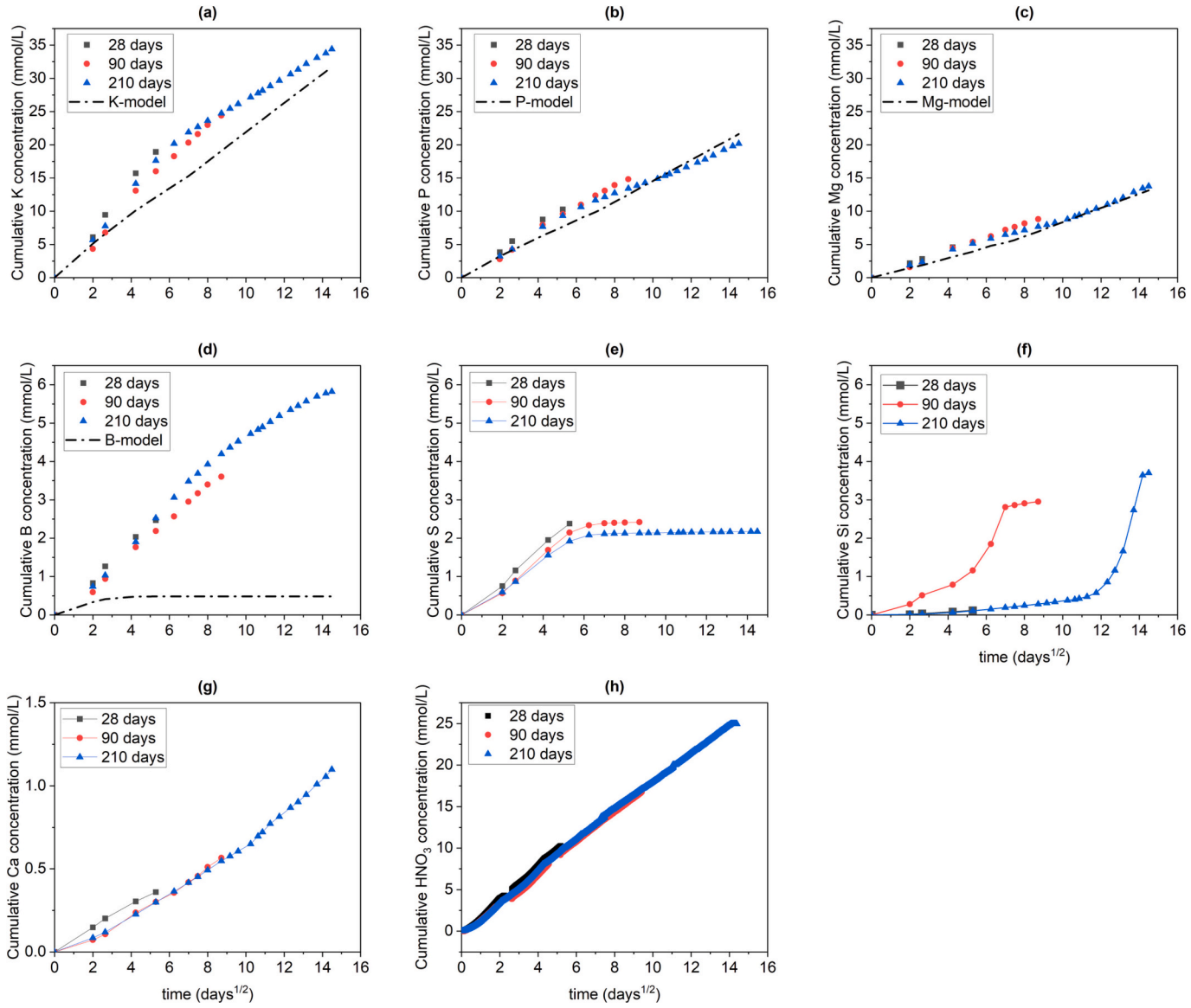

Fig. 7. Cumulative concentrations (in mmol/L) of leached species as a function of the square root of time (in days$^{1/2}$). (a) K, (b) P, (c) Mg, (d) B, (e) S, (f) Si, (g) Ca, and (h) HNO_3 injected by titration. Dots: experimental data, dotted lines: concentrations calculated with the reactive transport model.

Table 5
Initial and leached elemental concentrations (in mmol/g of paste) and leached fractions (in mol%).

			Al	B	Ca	Fe	K	Mg	Na	P	S*	Si
Leaching time (days)		Initial concentration	1.9	0.1	0.3	0.6	2.8	2.4	0.1	2.6	0.0	3.8
	28	Leached concentration	0.0	0.1	0.01	0.0	0.4	0.1	0.003	0.2	0.1	0.003
		Leached fraction (%)	0.0	43.1	2.5	0.0	15.8	5.1	4.0	9.2	130.8	0.1
	90	Leached concentration	0.0	0.1	0.01	0.0	0.6	0.2	0.01	0.3	0.1	0.1
		Leached fraction (%)	0.0	62.9	3.9	0.0	20.3	8.6	6.6	13.2	132.8	1.8
	210	Leached concentration	0.0	0.13	0.03	0.0	0.79	0.32	0.01	0.47	0.05	0.09
		Leached fraction (%)	0.0	101.7	7.6	0.0	28.6	13.4	8.8	18.0	119.5	2.2

* Note that the experimental error in S concentration determination by ICP-AES was significant (c.a. 15 %), resulting in a cumulative leached fraction higher than 100 % for this element.

Finally, the mullite-to-quartz ratio remained constant at about 3, meaning that these phases were resistant to leaching. Therefore, the dissolved Ca and Si observed in Fig. 7 likely resulted from partial dissolution of the vitreous phases in the fly ash.

3.2.2.2. ^{31}P and ^{11}B MAS-NMR analyses. Fig. 11 displays the ^{31}P and ^{11}B MAS-NMR spectra obtained from MKP-ref and MKP-90d. In the MKP-90d solid, the analyses were performed in a combination of zones 1 and 2 (corresponding to a layer of approximately 200 μm of material) as the amount of recovered powder was too small to analyze each zone separately.

The ^{31}P MAS-NMR spectrum of MKP-90d showed two main ^{31}P resonances (Fig. 11). The first narrow signal at δ = +6.6 ppm, corresponded to K-struvite. The second broad signal, identified from δ = +10

Table 6
Regression analyses of cumulative element concentrations (K, P, Mg and B) in leachates during the first stage of leaching (28 days), using the method of least-squares. Slopes (S) are reported in mmol·L^{-1}·d$^{-1/2}$ along with their corresponding standard deviations (S.D.) and correlations coefficients (r^2).

Test	1			2			3		
Element	Slope	S.D.	r^2	Slope	S.D.	r^2	Slope	S.D.	r^2
K	3.695	0.154	0.993	2.920	0.099	0.995	3.394	0.153	0.992
P	1.998	0.026	0.999	1.742	0.043	0.998	1.796	0.063	0.995
Mg	1.020	0.026	0.997	0.982	0.044	0.992	0.991	0.038	0.994
B	0.478	0.015	0.996	0.397	0.012	0.996	0.480	0.031	0.983
K/P	1.8			1.7			1.9		
K/Mg	3.6			3.0			3.4		
P/Mg	2.0			1.8			1.8		

1, 2 and 3 refer to the leaching tests carried out for 28, 90 and 210 days. Note that, for comparison, the slopes were calculated only using the first five points of each curve in Fig. 7.

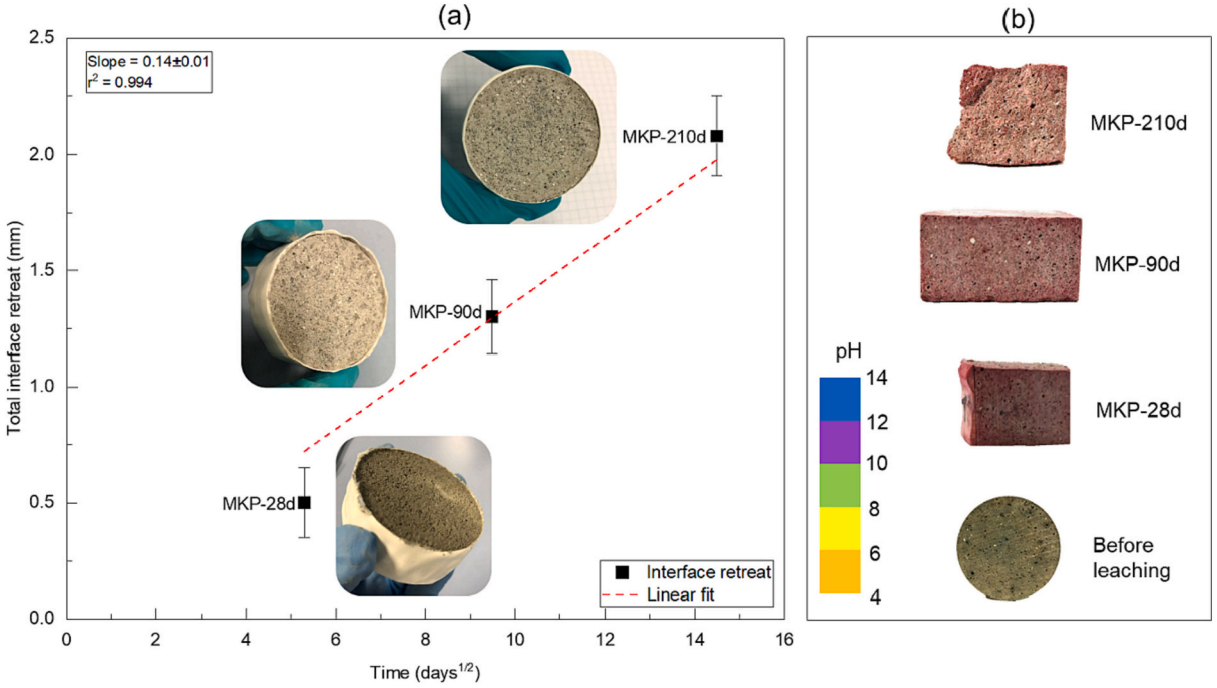

Fig. 8. (a) Interface retreat of leached solids (in mm) versus the square root of time (in days$^{1/2}$). Slope is given in mm·d$^{-1/2}$. The value of interface retreat includes the two exposed surfaces in the leached samples, and (b) estimation of pH on the cross-section of leached samples using the Rainbow indicator.

ppm to −5 ppm and centered at δ = +2.2 ppm indicated the presence of much less ordered ^{31}P environments. Note that different minerals could contribute to this broad resonance: cattiite (δ = +1.1 ppm) [38,44,45], and possibly amorphous orthophosphates ($Mg_3(PO4)_2.xH_2O$) at δ = +0.5 ppm. Site occupancies were assessed from spectrum decomposition (Table 4) and confirmed the decrease in the K-struvite content and the amorphization of the degraded zone due to leaching.

The ^{11}B MAS-NMR spectrum was noisy due to the small amount of B in the sample. Analyses of the leachates showed that about half of the boron content was released into the solution after 28 days (Table 5). Nonetheless, two different B environments were evidenced. The narrow resonance located at δ = +0.5 ppm was associated to B in 4-fold coordination (BO_4), while the broader signal centered around - 20 ppm corresponded to B in 3-fold coordination. These findings are consistent with previous studies [22,46]. Lahalle et al. [22] performed ^{31}P/^{11}B D-HMQC correlation experiments on MKPC solid fractions at different stages of hydration and found a correlation between orthophosphate and BO_4 moieties, but none between PO_4 and BO_3 groups. These results suggested the precipitation of a borophosphate mineral containing 4-fold coordinated boron. Regarding the 3-fold coordinated boron, it could result from adsorption of $B(OH)_3$ onto residual MgO or precipitated hydrates, or from the formation of a Mg or K borate phase without any phosphates. The fraction of B in 3-fold coordination seemed to increase slightly in the degraded zone, suggesting partial dissolution of the borophosphate phase.

3.2.2.3. SEM/EDS analyses. Fig. 12 presents a SEM image and EDS elemental mappings (K, Mg, P, Ca, Al, Si) of MKP-28d. Fig. 13 displays SE images obtained from a fracture cross-section of MKP-210d.

Figs. 12 and 13 provide insights into the distinct features of zone 1 (residual layer) and zone 2 (intermediate zone). The residual layer was thinner (with irregular thickness) and less dense than zone 2. It was mainly composed of fly ash, as confirmed by EDS mapping of Ca, Al, and Si (Fig. 12b) and by the morphology of fly ash grains shown in Fig. 13b. EDS mapping of K, P, and Mg (Fig. 12c) showed a decrease in elemental concentration in the residual layer, which explains the poor cohesion of this layer and its erosion into solution. K-struvite was not identified in zone 1, in agreement with XRD results (Fig. 9). Zone 2 exhibited some regions with lower concentrations in K but rich in Mg and P. This result was consistent with the precipitation of cattiite, which exhibited plate-like crystals (1–2 mm long) surrounded by small (10–30 μm long) rod-shaped crystals of K-struvite (Fig. 13a to c), similar to those reported by Li et al. [47].

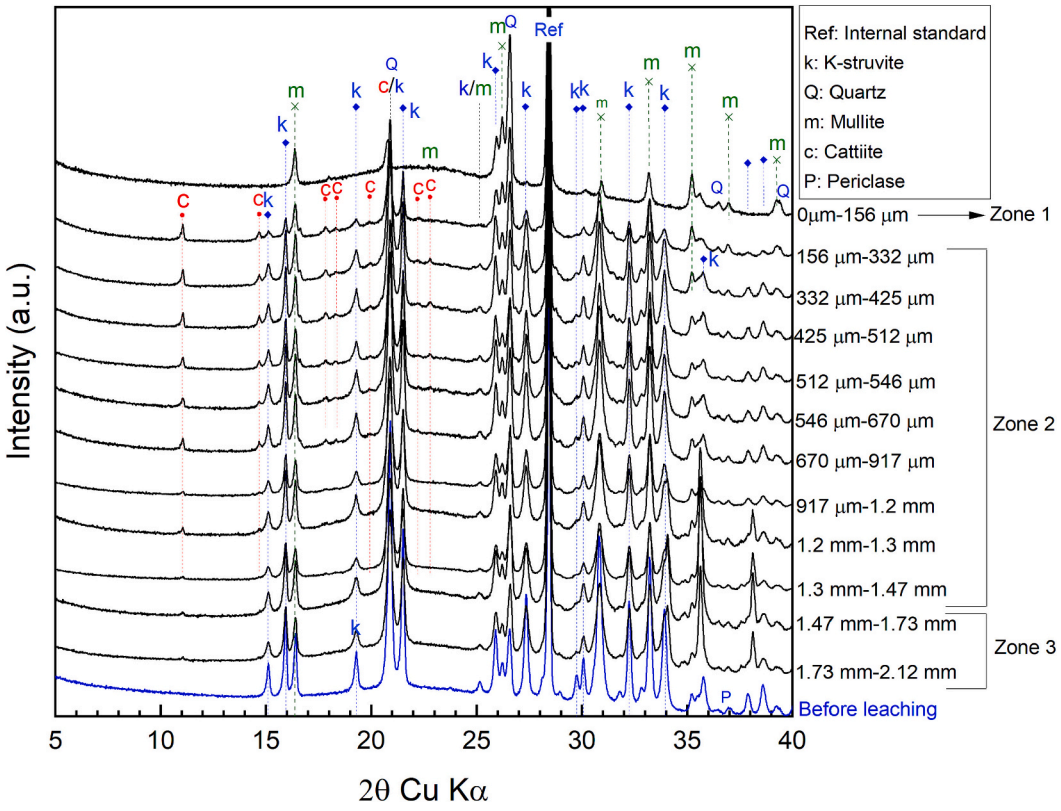

Fig. 9. XRD patterns of MKP-ref (blue pattern in the bottom) and MKP-28d (at different depths from the leached surface). (For interpretation of the references to color in this figure legend, the reader is referred to the web version of this article.)

Fig. 5b, c and d shows EDS mixing diagrams of analyses performed on the residual layers and intermediate zones of MKP-28d, MKP-90d and MKP-210d. The population of EDS points around K-struvite atomic ratios indicated that K-struvite was still present in the leached solids. Additionally, no dispersion of EDS points were observed towards residual KH_2PO_4, as observed prior to leaching (Fig. 5a). This result indicates that residual KH_2PO_4, present in MKP-ref (Fig. 3 and Table 4), was fully exhausted and leached into solution, which contributed to explain the inflection observed in the cumulative concentration curves of K and P (Fig. 7).

Moreover, EDS data confirmed the precipitation of new phases with low K content. The Mg/P atomic ratio of these phases ranged from 0.5 to 1.5, corresponding to cattiite ($Mg_3(PO_4)_2{\cdot}22H_2O$), but also, possibly, to other phases with lower Mg/P atomic ratios such as newberyite or magnesium hydrogen phosphates like $Mg(H_2PO_4)_2{\cdot}xH_2O$ or $MgH_2P_2O_7$ [48]. However, these phases were not identified by XRD nor by ^{31}P MAS-NMR, possibly because their content was below the detection limit.

Fig. 14 summarizes the zonation process identified in leached solids.

3.3. Leaching of MKPC paste samples: modeling

3.3.1. Paste composition before leaching

The composition of the 6-month old MKPC paste was simplified for modeling. The solid fraction was assumed to be composed of K-struvite, residual KH_2PO_4, MgO, as well as fly ash. MgO and fly ash were considered as non-reactive. The initial porosity of the paste was set at 15.5 %, as determined experimentally, and the pore network was considered as fully saturated. The composition of the pore solution was determined after extraction by pressing of the MKPC paste before leaching (K = 1033.8 mmol/L, *P* = 370 mmol/L, B = 136.4 mmol/L and Mg = 1.1 mmol/L, pH = 8.0). Note that after 6 months, the solution was still oversaturated with respect to K-struvite (saturation index = 0.87). To match the composition of the pore solution determined experimentally. Additional soluble salts were added in the initial assemblage (Table 7).

3.3.2. Modeling results

3.3.2.1. Leachates composition. No clear experimental value for the effective diffusion coefficient (D_e) was found in the literature that matched with the investigated MKPC formulation [7,49,50]. Therefore, a value of 1.7×10^{-11} $m^2{\cdot}s^{-1}$ was adjusted for the D_e to reproduce the leached cumulative concentrations of magnesium determined experimentally. It should be noted, however, that the fitted D_e value may not precisely match the experimental one, as the model neglected the dissolution of residual MgO and the presence of Mg-containing phases (e.g., $Mg_2KH(PO_4)_2{\cdot}15H_2O$), which could also contribute to the release of Mg^{2+} ions into the leachates. Nevertheless, using this value, the model successfully reproduced the overall trends for the leached cumulative concentrations of K and P, although the calculated concentrations were slightly underestimated. These underestimations may be attributed, once more, to the simplified composition considered for the cement paste, which neglected the contribution of impurities, fly ash, residual KH_2PO_4 and other phosphate phases that may be present in the solid (e.g., in the amorphous phase).

A major discrepancy was observed between the experimental and calculated B concentrations (Fig. 7d). Experimentally, B was gradually released from the paste and it was depleted after 210 days of leaching, whereas the model predicted a much faster exhaustion of B in 39 days only. Again, the bias in the model likely resulted from oversimplification of the paste composition. Boron was indeed added as soluble boric acid whereas experimental characterizations have shown that B partly precipitated as borophosphate phases of lower solubility [22]. One of these phases might be lünebergite ($Mg_3B_2(PO_4)_2(OH)_6{\cdot}6H_2O$) [51,52]. Given the absence of any experimental thermodynamic data for lünebergite, W. Han et al. [36] assessed its log *K* value using a uniform group

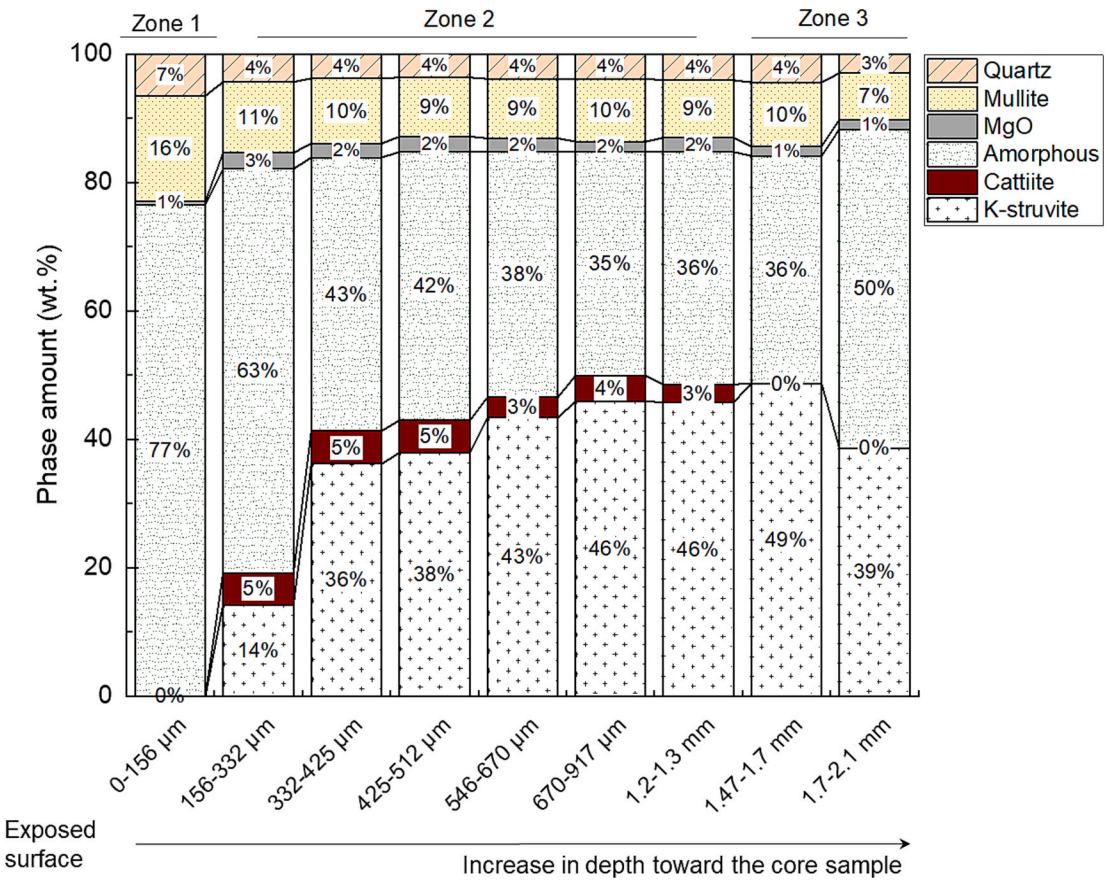

Fig. 10. Phase evolution in MKP-28d determined by Rietveld refinement.

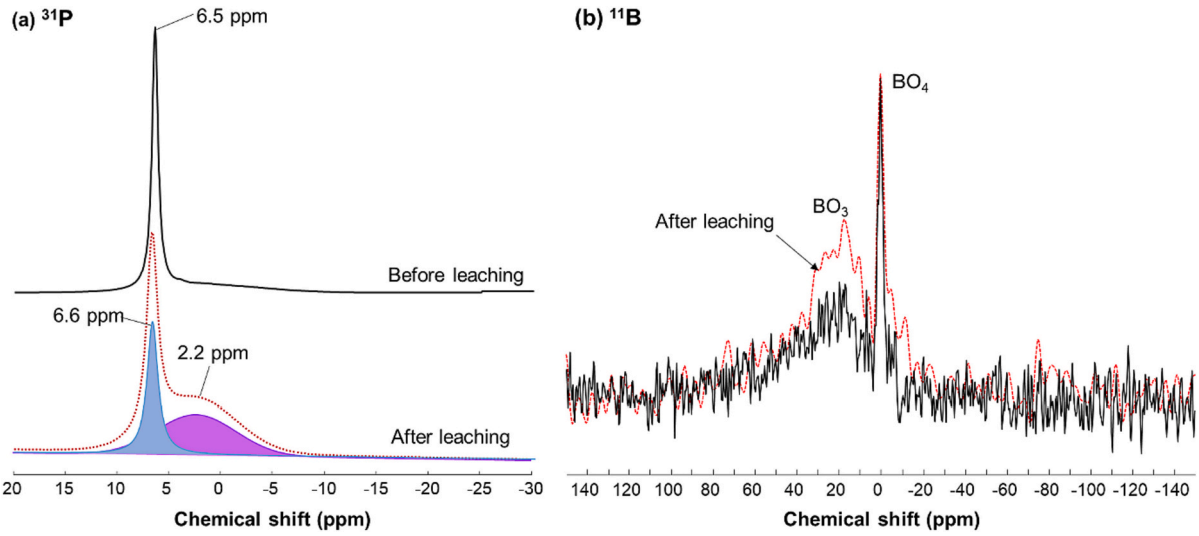

Fig. 11. MAS-NMR spectra of MKP-ref and MKP-90d (a) ^{31}P, and (b) ^{11}B. Colored lines correspond to single sites evidenced by decomposition.

contribution approach (Table 3). Therefore, a simulation was performed assuming that boron was initially precipitated as lünebergite. Nevertheless, with the *log K* value associated (Table 3), boron remained highly soluble and lünebergite was still fully dissolved at around 39 days. An experimental determination of the *log K* value of lünebergite would be necessary to confirm the calculated one. If so, this result may suggest another speciation than lünebergite for boron in the cement paste. This would agree with the conclusions reported by Lahalle et al. [22] who characterized some MKPC paste samples by ^{31}P and ^{11}B MAS-NMR. The ^{31}P/^{11}B correlation maps showed that if the formation of poorly crystallized lünebergite could not be ruled out, another mineral containing tetragonal boron connected to two orthophosphate groups also precipitated in the cement paste.

3.3.2.2. Cement paste composition. Fig. 15 displays the evolution of the paste calculated by modeling at 0, 28, 90 and 210 days of leaching. The calculated evolution of the mineral concentrations (K-struvite, cattiite and brucite) are given in mol/L of interstitial solution. The values of

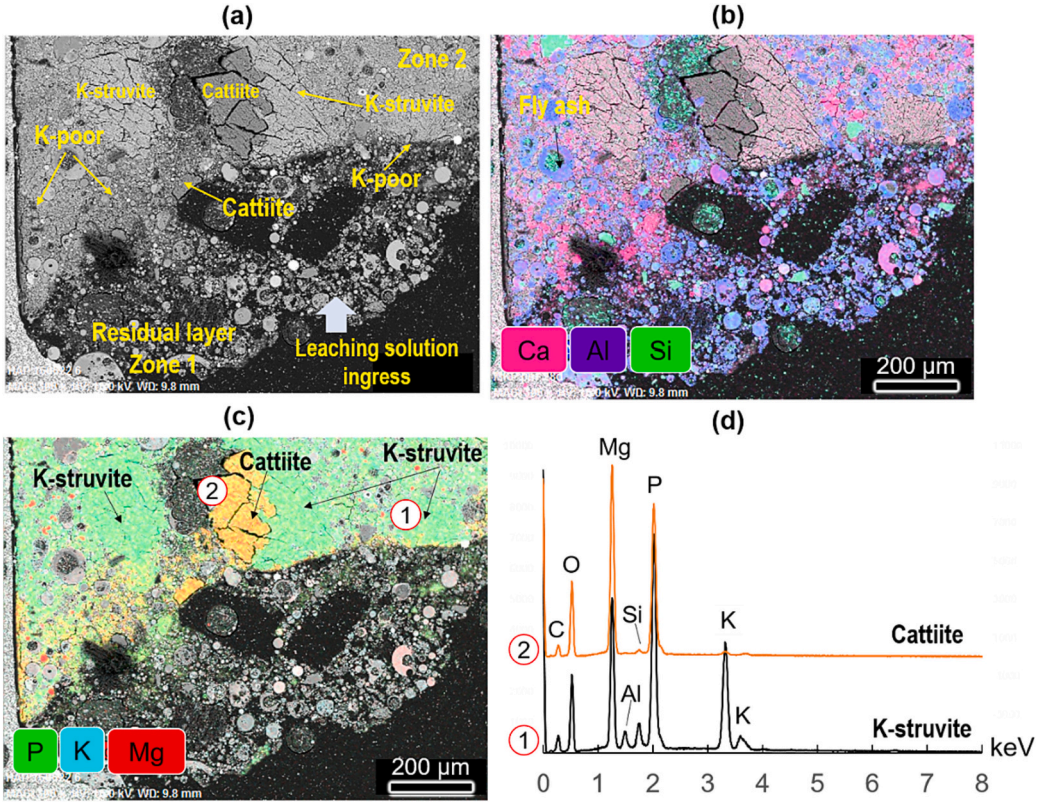

Fig. 12. MKP-28d characterization (a) SEM image, and (b) EDS elemental mapping of Ca, Al, Si, and (c) P, K, Mg. (d) EDS spectra obtained from target point areas showing (1) K-struvite, and (2) cattiite.

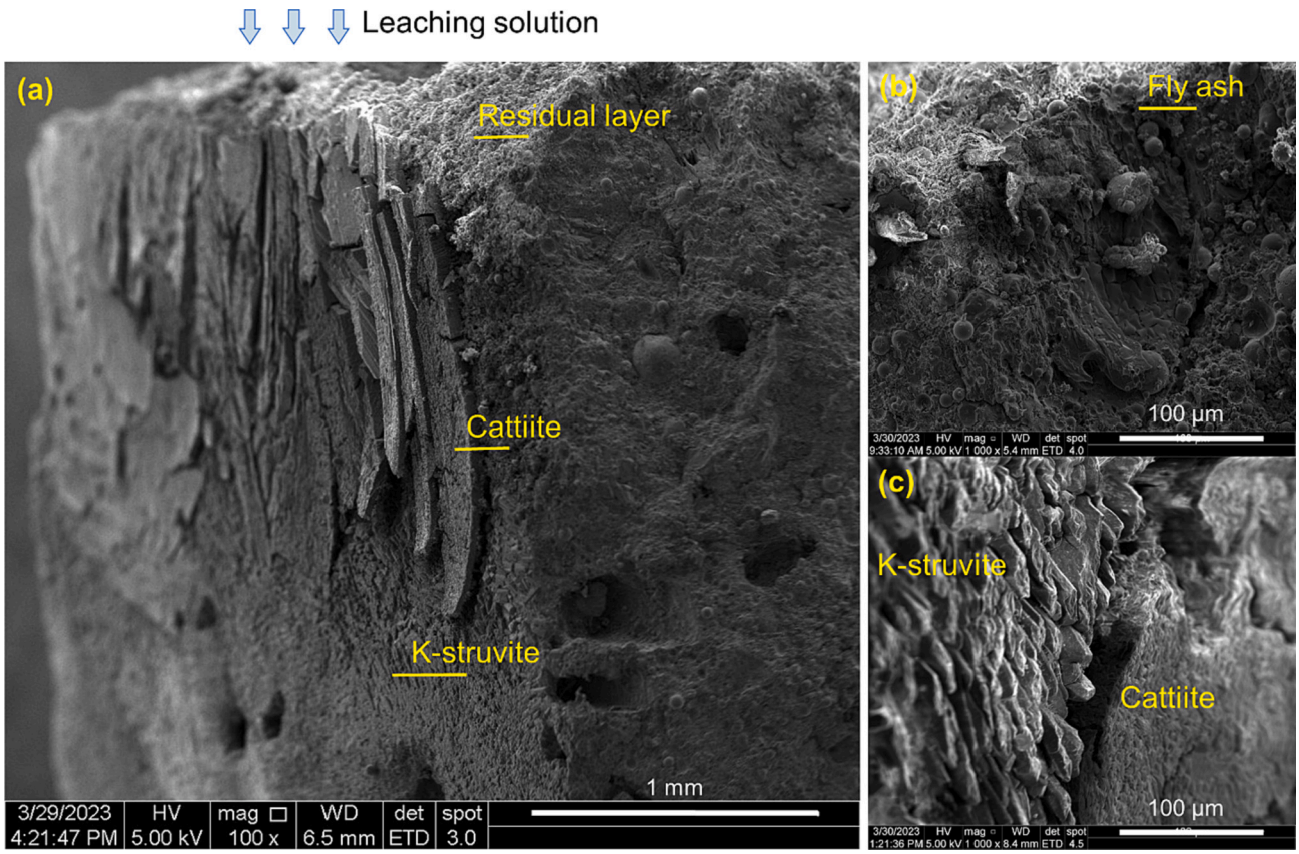

Fig. 13. MKP-210d (a) SE image of a fracture cross-section, (b) zoom-in on the residual layer, and (c) zoom-in on a K-struvite and cattiite interface.

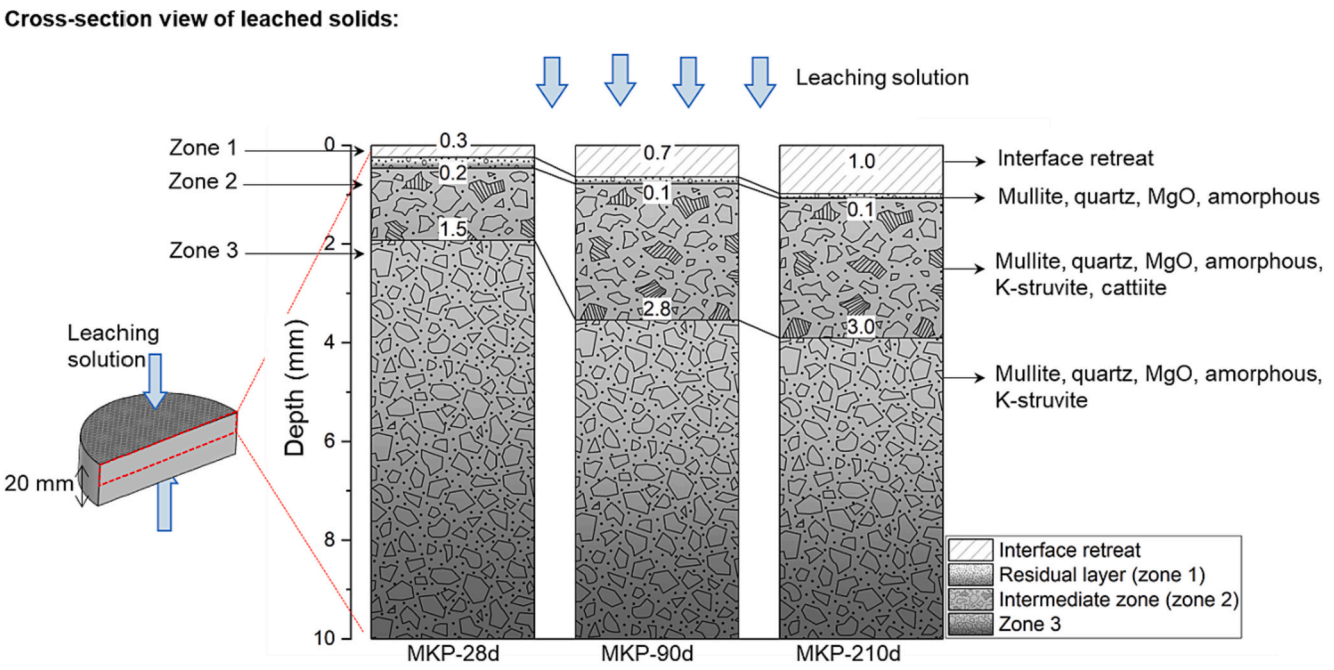

Fig. 14. Scheme of zonation process identified experimentally in leached solids.

Table 7
Parameters used to define the initial composition of the MKPC paste in the model. Concentrations are given in mmol/L of interstitial solution.

$MgKPO_4{\cdot}6H_2O$	KH_2PO_4	$B(OH)_3$	K_2O	Na_2O*
20,700	565	135	237	50

*Na_2O was added to adjust the pH at 8.0. Na_2O and K_2O are fictive species which fully dissolve, thus providing Na^+, K^+ and OH^- ions to the pore solution.

effective diffusion coefficient (D_e) are displayed in a Y-axis logarithmic scale.

The model predicted an interface retreat of the leached solid, which increased with the leaching time (Fig. 15a, d, g, and j), as observed experimentally. At 210 days, the calculated retreat reached 1.15 mm, which was consistent with the experimental determination given the experimental uncertainty (1.0 ± 0.2 mm, see Fig. 14).

The model also reproduced fairly well the phase evolution, with the dissolution of K-struvite and the precipitation of cattiite, providing that formation of bobierrite ($Mg_3(PO_4)_2{\cdot}8H_2O$) and magnesium orthophosphate tetrahydrate ($Mg_3(PO_4)_2.4H_2O$) was excluded. These two minerals are more stable than cattiite from a thermodynamical point of view [21]. However, they were not detected experimentally in the solid, suggesting that their formation was kinetically hindered at room temperature. Modeling predicted a pH increase in the leached solid, as evidenced experimentally with the Rainbow indicator (Fig. 8). In the simulation, the rise in pH could result from the fast depletion of borate ions, which contribute to buffer the pH in the range 8–9, and from the conversion of K-struvite into cattiite, releasing basic PO_4^{3-} anions (Eq. (4)).

$$3(MgKPO_4{\cdot}6H_2O) + 4H_2O \rightarrow Mg_3(PO_4)_2{\cdot}22H_2O + PO_4^{3-} + 3K^+ \quad (4)$$

When the pH reached 10.5, the model predicted the precipitation of brucite in the solid. This zone of brucite precipitation was narrower than that of cattiite, as the pH rapidly decreased to 7 at the interface, falling outside the stability domain of brucite. Destabilization of brucite was accompanied by transient reprecipitation of cattiite. Brucite precipitation predicted by the model, was however not evidenced experimentally. Additional characterization of the leached samples (not shown here) were performed using thermogravimetry analysis. No weight loss was observed in the 350–400 °C temperature range characteristic of brucite decomposition into periclase [53]. Different hypotheses might explain this deviation between experiment and modeling.

- Because of the residual presence of borate ions over the 210 days of leaching, the experimental pH rise would be slightly lower than the calculated one, and the stability domain of $Mg(OH)_2$ would not be reached.
- Precipitation of brucite would be kinetically hindered.
- Other nanocrystalline or amorphous Mg-containing phases, such as M-S-H [54] or magnesium borate [55] phases, might precipitate experimentally. These phases were not included in the simplified thermodynamic database used for modeling.

Speciation of Mg in the leached samples would deserve deeper investigation. Finally, the strong increase in porosity and effective diffusion coefficient was associated with the dissolution of K-struvite, despite the precipitation of cattiite. This increase in porosity may explain the very fragile nature of the external layer of the leached samples.

4. Discussion: degradation mechanisms of MKPC paste samples under leaching - comparison to conventional cementitious materials and insights for enhanced durability

Degradation of MKPC and Portland cement pastes under leaching involve a combination of diffusive transport and chemical reactions. Diffusion of the dissolved species in the pore network appears as the rate-limiting step for both materials when leaching is performed at pH 7 under dynamic conditions. As a consequence, a zonation process is observed, involving dissolution/precipitation fronts. In the MKPC cement paste, dissolution of K-struvite is accompanied by the transient precipitation of cattiite. In the Portland cement paste, the successive dissolution of portlandite, monosulfate (with transient reprecipitation of ettringite), ettringite and C-S-H phases is observed [56]. However, the extent of degradation at similar leaching times, is more important for the MKPC sample than for a Portland cement paste (w/c = 0.4) having initially a slightly higher water porosity (c.a. 25 vol%). After 90 days of leaching, the degradation front reaches 3.6 mm (including an interface

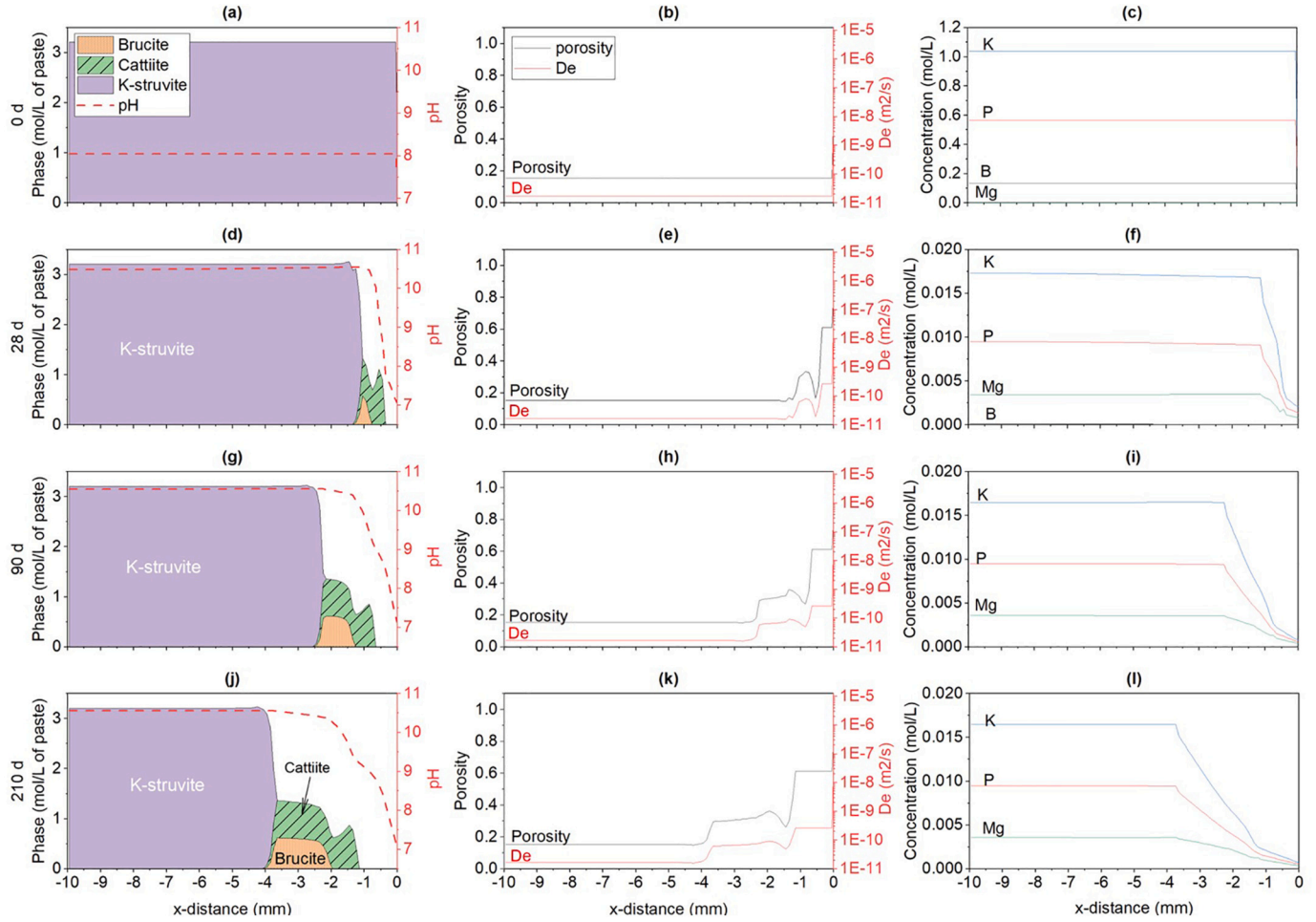

Fig. 15. Predicted evolution of the paste at different stages of leaching, (left) mineral concentration and pH, (middle) porosity and effective diffusion coefficient (De), (right) B, K, P and Mg concentrations.

retreat of 0.7 mm) for the MKPC paste, against 1.4 mm for the Portland cement paste [57]. The weaker resistance of the MKPC paste to leaching results from at least two factors: a higher diffusion coefficient, which may result from a higher fraction of macropores than in the Portland cement paste [58], and the presence of highly soluble phases (residual KH_2PO_4, impurities such as K_2SO_4), which are readily leached out, thus increasing the total porosity and diffusion coefficient. To improve the durability of MKPC materials, two complementary approaches may be foreseen:

- Increase the Mg/P molar ratio of the cement [27] to ensure total depletion of KH_2PO_4. An optimum should be found however to avoid the presence of excessive unreacted magnesia that raises the concern of brucite ($Mg(OH)_2$) formation in the long term and its possible detrimental influence on volume stability.
- Add a filler to modify the microstructure of the paste and thus, its transport properties. These properties are not only dependent on the total porosity but also on factors like the pore size distribution, tortuosity, and constrictivity within the cement matrix [59–62]. As an example, a simulation carried out in this study, demonstrated that reducing the effective diffusion coefficient (D_e) from 1.7×10^{-11} m^2/s to 3×10^{-12} m^2/s, a value commonly used for modeling Portland cement-based materials with a water-to-cement (w/c) ratio of 0.5 [32,34,63,64], could limit the extent of degradation to 0.85 mm after 90 days of leaching.

5. Conclusion

This investigation was focused on the leaching behavior of magnesium potassium phosphate cement (MKPC) pastes. MKPC paste samples were prepared using a Mg/P molar ratio of 1. After endogenous curing (20 °C), three semi-dynamic leaching tests were performed over 28 d, 90 d and 210 d on paste monoliths using demineralized water with a pH maintained at 7 by automatic titration. The leaching solutions were periodically renewed and the leachates were analyzed using ICP-AES. The leached solids were characterized by XRD, SEM/EDS, and ^{31}P and ^{11}B MAS-NMR. The main conclusions drawn from this study are summarized as follows.

- Degradation of MKPC samples under leaching can be defined as a combination of diffusive transport and chemical reactions (dissolution/precipitation fronts), with diffusion as the rate limiting process, as evidenced by the linear evolution of cumulative leached element concentrations versus the square root of time.
- Degradation of MKPC paste samples increased continuously with the leaching time over the investigated period (210 d).
- All leached samples showed a zonation process: K-struvite was dissolved at the exposed surface of the samples, followed by an intermediate zone, where K-struvite and cattiite coexisted, and finally a third zone where cattiite was not identified anymore.
- Based on these results, a first modeling approach using reactive transport was proposed and helped to gain insights into the degradation process of MKPC materials under leaching. It reproduced

fairly well the mineralogical changes observed experimentally, except for the precipitation of brucite which was predicted by the model, but not evidenced in the leached samples.

To improve the simulations, future work should focus on:

- The determination of the diffusion coefficient of MKPC pastes as a function of their formulation parameters to confirm the adjusted values currently used for modeling.
- The identification of the borate minerals precipitating in the MKPC paste and the determination of their solubility product.

Besides, the approach used in this study, combining experimentation under well-controlled conditions and modeling, should be extended to the investigation of MKPC pastes with Mg/P molar ratio higher than 1 to determine the influence on this parameter on their degradation process. Finally, since MKPC-based materials are potential candidates for the stabilization/solidification of waste containing aluminum metal, the magnitude of the pH increase induced by leaching should be evaluated more precisely, as well as its influence on the corrosion rate of Al metal.

CRediT authorship contribution statement

Laura Diaz Caselles: Conceptualization, Formal analysis, Investigation, Methodology, Project administration, Software, Writing – original draft. **Céline Cau Dit Coumes:** Conceptualization, Funding acquisition, Project administration, Resources, Supervision, Validation, Writing – review & editing. **Pascal Antonucci:** Investigation. **Angélique Rousselet:** Conceptualization, Validation, Writing – review & editing. **Adel Mesbah:** Formal analysis, Software, Writing – review & editing. **Valérie Montouillout:** Formal analysis, Investigation, Validation, Writing – review & editing.

Declaration of competing interest

The authors declare the following financial interests/personal relationships which may be considered as potential competing interests:

Laura Diaz Caselles reports financial support was provided by EU Framework Programme for Research and Innovation Euratom. If there are other authors, they declare that they have no known competing financial interests or personal relationships that could have appeared to influence the work reported in this paper.

Data availability

Data will be made available on request.

Acknowledgements

This project has received funding from the European Union's Horizon 2020 research and innovation programme for Nuclear Fission and Radiation Protection Research (Call NFRP-2019-2020) under grant agreement No. 945098 (PREDIS).

Many thanks are given to Laurent De Windt (Mines Paris) for the assistance with HYTEC modeling.

References

[1] F.P. Glasser, Progress in the immobilization of radioactive wastes in cement, Cem. Concr. Res. 22 (1992) 201–216, https://doi.org/10.1016/0008-8846(92)90058-4.
[2] L. Ionascu, M. Nicu, C. Turcanu, F. Dragolici, G.H. Rotarescu, Study of the conditioning matrices for aluminium radioactive wastes, Rom. J. Phys. 59 (2014) 360–368.
[3] C. Cau Dit Coumes, D. Lambertin, H. Lahalle, P. Antonucci, C. Cannes, S. Delpech, Selection of a mineral binder with potentialities for the stabilization/solidification of aluminum metal, J. Nucl. Mater. 453 (2014) 31–40, https://doi.org/10.1016/j.jnucmat.2014.06.032.
[4] S. Delpech, C. Cannes, N. Barré, Q.T. Tran, C. Sanchez, H. Lahalle, D. Lambertin, S. Gauffinet, C.C.D. Coumes, Kinetic model of aluminum behavior in cement-based matrices analyzed by impedance spectroscopy, J. Electrochem. Soc. 164 (2017) C717–C727, https://doi.org/10.1149/2.0211713jes.
[5] H. Lahalle, Conditionnement de l'aluminium métallique dans les ciments phospho-magnésiens, Université de Bourgogne, 2016.
[6] I. Buj, J. Torras, M. Rovira, J. de Pablo, Leaching behaviour of magnesium phosphate cements containing high quantities of heavy metals, J. Hazard. Mater. 175 (2010) 789–794, https://doi.org/10.1016/j.jhazmat.2009.10.077.
[7] J. Torras, I. Buj, M. Rovira, J. de Pablo, Semi-dynamic leaching tests of nickel containing wastes stabilized/solidified with magnesium potassium phosphate cements, J. Hazard. Mater. 186 (2011) 1954–1960, https://doi.org/10.1016/j.jhazmat.2010.12.093.
[8] J.Y. Pyo, W. Um, J. Heo, Magnesium potassium phosphate cements to immobilize radioactive concrete wastes generated by decommissioning of nuclear power plants, Nucl. Eng. Technol. 53 (2021) 2261–2267, https://doi.org/10.1016/j.net.2021.01.005.
[9] J. Li, W. Zhang, Y. Cao, Laboratory evaluation of magnesium phosphate cement paste and mortar for rapid repair of cement concrete pavement, Constr. Build. Mater. 58 (2014) 122–128, https://doi.org/10.1016/j.conbuildmat.2014.02.015.
[10] A. Arora, B. Singh, P. Kaur, Novel material i.e. magnesium phosphate cement (MPC) as repairing material in roads and buildings, Mater. Today Proc. 17 (2019) 70–76, https://doi.org/10.1016/j.matpr.2019.06.402.
[11] S.S. Seehra, S. Gupta, S. Kumar, Rapid setting magnesium phosphate cement for quick repair of concrete pavements - characterisation and durability aspects, Cem. Concr. Res. 23 (1993) 254–266, https://doi.org/10.1016/0008-8846(93)90090-V.
[12] Y. Yu, J. Wang, C. Liu, B. Zhang, H. Chen, H. Guo, G. Zhong, W. Qu, S. Jiang, H. Huang, Evaluation of inherent toxicology and biocompatibility of magnesium phosphate bone cement, Colloids Surf. B: Biointerfaces 76 (2010) 496–504, https://doi.org/10.1016/j.colsurfb.2009.12.010.
[13] Y. Yu, C. Xu, H. Dai, Preparation and characterization of a degradable magnesium phosphate bone cement, Regen. Biomater. 3 (2016) 231–237, https://doi.org/10.1093/rb/rbw024.
[14] Z. Zhang, Z. Yang, Z. Chen, T. Kang, X. Ding, Y. Li, Y. Liao, C. Chen, H. Yuan, H. Peng, A study on bone cement containing magnesium potassium phosphate for bone repair, Cogent Biol. 4 (2018) 1487255, https://doi.org/10.1080/23312025.2018.1487255.
[15] B. Weill, J. Bradik, US Patent n°4,756,762 - Magnesium phosphate cement systems, 1988.
[16] A.S. Wagh, S.-Y. Jeong, D. Singh, High strength phosphate cement using, in: Proc. 1st Int. Conf. High Strength Concr, 1997, pp. 542–553.
[17] A.S. Wagh, Recent progress in chemically bonded phosphate ceramics, ISRN Ceram. 2013 (2013) 1–20, https://doi.org/10.1155/2013/983731.
[18] B. Xu, B. Lothenbach, A. Leemann, F. Winnefeld, Reaction mechanism of magnesium potassium phosphate cement with high magnesium-to-phosphate ratio, Cem. Concr. Res. 108 (2018) 140–151, https://doi.org/10.1016/j.cemconres.2018.03.013.
[19] Z. Ding, B. Dong, F. Xing, N. Han, Z. Li, Cementing mechanism of potassium phosphate based magnesium phosphate cement, Ceram. Int. 38 (2012) 6281–6288, https://doi.org/10.1016/j.ceramint.2012.04.083.
[20] B. Xu, F. Winnefeld, J. Kaufmann, B. Lothenbach, Influence of magnesium-to-phosphate ratio and water-to-cement ratio on hydration and properties of magnesium potassium phosphate cements, Cem. Concr. Res. 123 (2019) 105781, https://doi.org/10.1016/j.cemconres.2019.105781.
[21] B. Lothenbach, B. Xu, F. Winnefeld, Thermodynamic data for magnesium (potassium) phosphates, Appl. Geochem. 111 (2019) 104450, https://doi.org/10.1016/j.apgeochem.2019.104450.
[22] H. Lahalle, C. Cau Dit Coumes, C. Mercier, D. Lambertin, C. Cannes, S. Delpech, S. Gauffinet, Influence of the w/c ratio on the hydration process of a magnesium phosphate cement and on its retardation by boric acid, Cem. Concr. Res. 109 (2018) 159–174, https://doi.org/10.1016/j.cemconres.2018.04.010.
[23] H. Lahalle, C. Patapy, M. Glid, G. Renaudin, M. Cyr, Microstructural evolution/durability of magnesium phosphate cement paste over time in neutral and basic environments, Cem. Concr. Res. 122 (2019) 42–58, https://doi.org/10.1016/j.cemconres.2019.04.011.
[24] Q. Yang, B. Zhu, X. Wu, Characteristics and durability test of magnesium phosphate cement-based material for rapid repair of concrete, Mater. Struct. Constr. 33 (2000) 229–234, https://doi.org/10.1007/bf02479332.
[25] Y. Li, B. Chen, Factors that affect the properties of magnesium phosphate cement, Constr. Build. Mater. 47 (2013) 977–983, https://doi.org/10.1016/j.conbuildmat.2013.05.103.
[26] L. Chong, J. Yang, C. Shi, Effect of curing regime on water resistance of magnesium–potassium phosphate cement, Constr. Build. Mater. 151 (2017) 43–51, https://doi.org/10.1016/j.conbuildmat.2017.06.056.
[27] M. Le Rouzic, T. Chaussadent, L. Stefan, M. Saillio, On the influence of Mg/P ratio on the properties and durability of magnesium potassium phosphate cement pastes, Cem. Concr. Res. 96 (2017) 27–41, https://doi.org/10.1016/j.cemconres.2017.02.033.
[28] R. Snellings, J. Chwast, Ö. Cizer, N. De Belie, Y. Dhandapani, P. Durdzinski, J. Elsen, J. Haufe, D. Hooton, C. Patapy, M. Santhanam, K. Scrivener, D. Snoeck, L. Steger, S. Tongbo, A. Vollpracht, F. Winnefeld, B. Lothenbach, RILEM TC-238 SCM recommendation on hydration stoppage by solvent exchange for the study of hydrate assemblages, Mater. Struct. Constr. 51 (2018), https://doi.org/10.1617/s11527-018-1298-5.

[29] C. Frontera, J. Rodríguez-Carvajal, FullProf as a new tool for flipping ratio analysis, Phys. B Condens. Matter 335 (2003) 219–222, https://doi.org/10.1016/S0921-4526(03)00241-2.
[30] D. Massiot, F. Fayon, M. Capron, I. King, S. Le Calvé, B. Alonso, J.-O. Durand, B. Bujoli, Z. Gan, G. Hoatson, Modelling one- and two-dimensional solid-state NMR spectra, Magn. Reson. Chem. 40 (2002) 70–76, https://doi.org/10.1002/mrc.984.
[31] J. van der Lee, L. De Windt, V. Lagneau, P. Goblet, Module-oriented modeling of reactive transport with HYTEC, Comput. Geosci. 29 (2003) 265–275, https://doi.org/10.1016/S0098-3004(03)00004-9.
[32] L. De Windt, R. Badreddine, Modelling of long-term dynamic leaching tests applied to solidified/stabilised waste, Waste Manag. 27 (2007) 1638–1647, https://doi.org/10.1016/j.wasman.2006.07.019.
[33] N. Neithalath, J. Weiss, J. Olek, Characterizing enhanced porosity concrete using electrical impedance to predict acoustic and hydraulic performance, Cem. Concr. Res. 36 (2006) 2074–2085, https://doi.org/10.1016/j.cemconres.2006.09.001.
[34] L. De Windt, P. Devillers, Modeling the degradation of Portland cement pastes by biogenic organic acids, Cem. Concr. Res. 40 (2010) 1165–1174, https://doi.org/10.1016/j.cemconres.2010.03.005.
[35] F. Adenot, M. Buil, Modelling of the corrosion of the cement paste by deionized water, Cem. Concr. Res. 22 (1992) 489–496.
[36] W. Han, H. Chen, X. Li, T. Zhang, Thermodynamic modeling of magnesium ammonium phosphate cement and stability of its hydration products, Cem. Concr. Res. 138 (2020) 106223, https://doi.org/10.1016/j.cemconres.2020.106223.
[37] L.J. Gardner, S.A. Bernal, S.A. Walling, C.L. Corkhill, J.L. Provis, N.C. Hyatt, Characterisation of magnesium potassium phosphate cements blended with fly ash and ground granulated blast furnace slag, Cem. Concr. Res. 74 (2015) 78–87, https://doi.org/10.1016/j.cemconres.2015.01.015.
[38] A. Viani, G. Mali, P. Mácová, Investigation of amorphous and crystalline phosphates in magnesium phosphate ceramics with solid-state 1H and 31P NMR spectroscopy, Ceram. Int. 43 (2017) 6571–6579, https://doi.org/10.1016/j.ceramint.2017.02.087.
[39] K.O. Kongshaug, H. Fjellvåg, K.P. Lillerud, The synthesis and crystal structure of a hydrated magnesium phosphate Mg3(PO4)2·4H2O, Solid State Sci. 3 (2001) 353–359, https://doi.org/10.1016/S1293-2558(00)01109-2.
[40] L.H. Merwin, A. Sebald, H. Rager, H. Schneider, 29Si and 27Al MAS NMR spectroscopy of mullite, Phys. Chem. Miner. 18 (1991), https://doi.org/10.1007/BF00199043.
[41] Á. Palomo, S. Alonso, A. Fernandez-Jiménez, I. Sobrados, J. Sanz, Alkaline activation of fly ashes: NMR study of the reaction products, J. Am. Ceram. Soc. 87 (2004) 1141–1145, https://doi.org/10.1111/j.1551-2916.2004.01141.x.
[42] I. Jaymes, A. Douy, D. Massiot, J.P. Coutures, Evolution of the Si environment in mullite solid solution by 29Si MAS-NMR spectroscopy, J. Non-Cryst. Solids 204 (1996) 125–134, https://doi.org/10.1016/S0022-3093(96)00414-0.
[43] G. Kunath-Fandrei, P. Rehak, S. Steuernagel, H. Schneider, C. Jäger, Quantitative structural analysis of mullite by 27Al nuclear magnetic resonance satellite transition spectroscopy, Solid State Nucl. Magn. Reson. 3 (1994) 241–248, https://doi.org/10.1016/0926-2040(94)90001-9.
[44] M.A. Aramendía, V. Borau, C. Jiménez, J.M. Marinas, F.J. Romero, J.R. Ruiz, XRD and solid-state nmr study of magnesium oxide–magnesium orthophosphate systems, J. Solid State Chem. 135 (1998) 96–102, https://doi.org/10.1006/jssc.1997.7602.
[45] S.N. Scrimgeour, J.A. Chudek, C.H. Lloyd, The determination of phosphorus containing compounds in dental casting investment products by 31P solid-state MAS-NMR spectroscopy, Dent. Mater. 23 (2007) 415–424, https://doi.org/10.1016/j.dental.2006.02.010.
[46] S. Elbers, W. Strojek, L. Koudelka, H. Eckert, Site connectivities in silver borophosphate glasses: new results from 11B{31P} and 31P{11B} rotational echo double resonance NMR spectroscopy, Solid State Nucl. Magn. Reson. 27 (2005) 65–76, https://doi.org/10.1016/j.ssnmr.2004.08.007.
[47] H. Li, S.-H. Yu, Q.-Z. Yao, G.-T. Zhou, S.-Q. Fu, Chemical control of struvite scale by a green inhibitor polyaspartic acid, RSC Adv. 5 (2015) 91601–91608, https://doi.org/10.1039/C5RA17149K.
[48] E. Qoku, M. Scheibel, T. Bier, A. Gerz, Phase development of different magnesium phosphate cements at room temperature and elevated temperatures, Constr. Build. Mater. 272 (2021) 121654, https://doi.org/10.1016/j.conbuildmat.2020.121654.
[49] X. Man, M. Aminul Haque, B. Chen, Engineering properties and microstructure analysis of magnesium phosphate cement mortar containing bentonite clay, Constr. Build. Mater. 227 (2019) 116656, https://doi.org/10.1016/j.conbuildmat.2019.08.037.
[50] R. Zhu, C. Ye, H. Xiang, R. Cheng, W. Tao, Z. Lin, Z. Xie, B. Liao, Study on the material characteristics and barrier mechanism of magnesium potassium phosphate cement/hydroxyapatite cutoff walls for fluoride contamination in phosphogypsum waste stacks, Constr. Build. Mater. 347 (2022) 128469, https://doi.org/10.1016/j.conbuildmat.2022.128469.
[51] E. Soudée, Liants phospho-magnésiens : mécanisme de prise et durabilité, INSA, Lyon, 1999.
[52] A.S. Wagh, D. Singh, S.Y. Jeong, Stabilization of hazardous ash waste with newberyite-rich chemically bonded magnesium phosphate ceramic, Illinois, n.d. https://digital.library.unt.edu/ark:/67531/metadc690720/: (accessed October 11, 2023).
[53] K.J.D. MacKenzie, R.H. Meinhold, Thermal decomposition of brucite, Mg(OH)2: a 25Mg MAS NMR study, Thermochim. Acta 230 (1993) 339–343, https://doi.org/10.1016/0040-6031(93)80371-G.
[54] E. Bernard, B. Lothenbach, D. Rentsch, I. Pochard, A. Dauzères, Formation of magnesium silicate hydrates (M-S-H), Phys. Chem. Earth, Parts A/B/C 99 (2017) 142–157, https://doi.org/10.1016/j.pce.2017.02.005.
[55] J. Li, S. Gao, S. Xia, B. Li, R. Hu, Thermochemistry of hydrated magnesium borates, J. Chem. Thermodyn. 29 (1997) 491–497, https://doi.org/10.1006/jcht.1996.0183.
[56] P. Faucon, F. Adenot, J. Jacquinot, J. Petit, R. Cabrillac, M. Jorda, Long-term behaviour of cement pastes used for nuclear waste disposal: review of physico-chemical mechanisms of water degradation, Cem. Concr. Res. 28 (1998) 847–857, https://doi.org/10.1016/S0008-8846(98)00053-2.
[57] F. Adenot, Durabilité du béton: caractérisation et modélisation des processus physiques et chimiques de dégradation du ciment, Orléans University, 1992.
[58] I. Odler, M. Rößler, Investigations on the relationship between porosity, structure and strength of hydrated Portland cement pastes. II. Effect of pore structure and of degree of hydration, Cem. Concr. Res. 15 (1985) 401–410, https://doi.org/10.1016/0008-8846(85)90113-9.
[59] G. Sun, W. Sun, Y. Zhang, Z. Liu, Relationship between chloride diffusivity and pore structure of hardened cement paste, J. Zhejiang Univ. A 12 (2011) 360–367, https://doi.org/10.1631/jzus.A1000413.
[60] Q.T. Phung, N. Maes, E. Jacops, D. Jacques, G. De Schutter, G. Ye, Insights and issues on the correlation between diffusion and microstructure of saturated cement pastes, Cem. Concr. Compos. 96 (2019) 106–117, https://doi.org/10.1016/j.cemconcomp.2018.11.018.
[61] B. Ghanbarian, A.G. Hunt, R.P. Ewing, M. Sahimi, Tortuosity in porous media: a critical review, Soil Sci. Soc. Am. J. 77 (2013) 1461–1477, https://doi.org/10.2136/sssaj2012.0435.
[62] X.B. Zuo, W. Sun, H. Li, W.J. Zhou, Geometrical model for tortuosity of transport paths in hardened cement pastes, Adv. Cem. Res. 24 (2012) 145–154, https://doi.org/10.1680/adcr.10.00042.
[63] K. Haga, S. Sutou, M. Hironaga, S. Tanaka, S. Nagasaki, Effects of porosity on leaching of Ca from hardened ordinary Portland cement paste, Cem. Concr. Res. 35 (2005) 1764–1775, https://doi.org/10.1016/j.cemconres.2004.06.034.
[64] S. Bejaoui, B. Bary, Modeling of the link between microstructure and effective diffusivity of cement pastes using a simplified composite model, Cem. Concr. Res. 37 (2007) 469–480, https://doi.org/10.1016/j.cemconres.2006.06.004.